EUROPEAN ORGANIZATION FOR NUCLEAR RESEARCH

L3 Note 2189
November 21, 1997

Study of the Photon Structure Function F_2^γ at LEP1

C.H. Lin
National Central University, Taiwan

Abstract

The photon structure function F_2^γ is studied in the reaction $e^+e^- \rightarrow e^+e^- hadrons$ at LEP with the L3 detector. The data is collected from 1991 to 1995 at center-of-mass energy $\sqrt{s} \simeq 91$ GeV, corresponding to the integrated luminosity 140 pb^{-1}. We measure the photon structure function F_2^γ at two Q^2 bins from 1.2 to 9.0 GeV. The x range is from 0.002 to 0.1 at $\langle Q^2 \rangle = 1.9$ GeV and from 0.005 to 0.2 at $\langle Q^2 \rangle = 5.0$ GeV.

1 Introduction and formalism

The photon structure function can be measured at e^+e^- storage rings via the two-photon interaction. This measurement has been performed at various e^+e^- experiments [1–4]. Fig. 1 shows the typical diagram of two-photon interaction. If one photon has high virtuality ($Q^2 \gg 0$) and the other is quasi-real ($P^2 \sim 0$), the interaction can be regarded as a deep inelastic scattering of an $e^\pm$ on the quasi-real photon. The flux of the quasi-real photon can be calculated by the Equivalent Photon Approximation (EPA) [5].

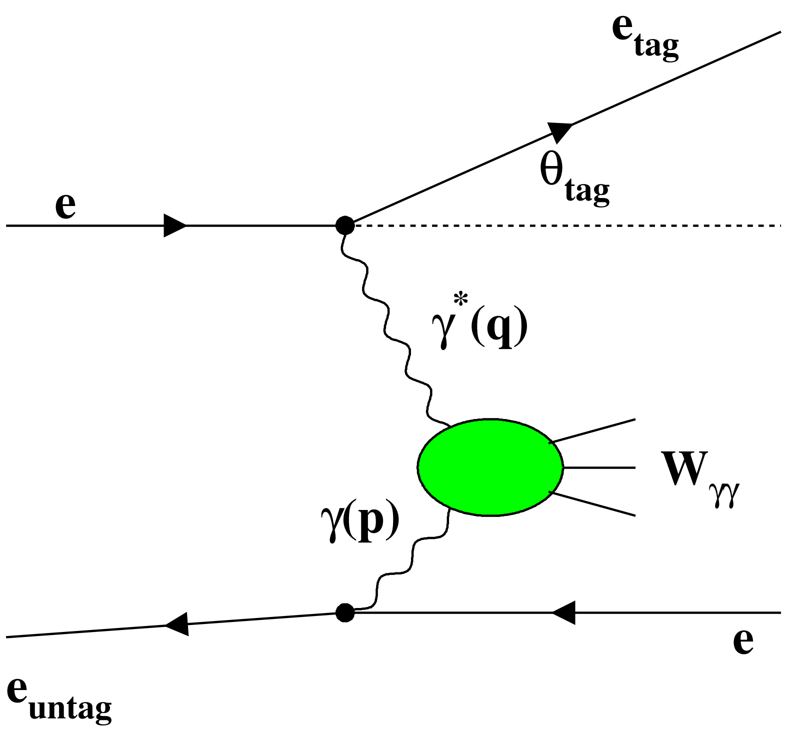

Figure 1: Diagram of two-photon interaction. The $Q^2 = -q^2$ and $P^2 = -p^2$ are the virtuality of photons. The $W_{\gamma\gamma}$ is the two-photon invariant mass.

The cross-section of the deep inelastic $e\gamma$ scattering is expressed as [5]:

$$\frac{d^2\sigma_{e\gamma\to e\mathrm{X}}}{dxdQ^2} = \frac{2\pi\alpha^2}{xQ^4}[(1+(1-y)^2)F_2^\gamma(x,Q^2) - y^2F_L^\gamma(x,Q^2)] \quad (1)$$

where

$$\begin{aligned} x &= \frac{Q^2}{Q^2+W_{\gamma\gamma}^2} \\ y &= 1 - \frac{E_{tag}}{E_{beam}}\cos^2\frac{\theta_{tag}}{2} \\ W_{\gamma\gamma} &= (q+p)^2 \end{aligned} \quad (2)$$

In the kinematic regime studied here ($E_{tag} \sim E_{beam}$), y^2 is very small ($\langle y \rangle \sim 0.08$). Therefore The measured cross-section is only sensitive to F_2^γ. The longitudinal structure function F_L^γ can be neglected.

The photon structure function is usually parameterised as:

$$F_2^\gamma = F_2^{PL} + F_2^{hadr} \tag{3}$$

where F_2^{PL} means that the photon interacts as a point-like particle and F_2^{hadr} means the photon is hadron-like. The point-like part can be calculated by the Quark Parton Model ($P^2 = 0$) [5]:

$$F_2^{\gamma,\ QPM}(x, Q^2) = \frac{3\alpha}{\pi} \cdot x \sum_q e_q^4 \{[x^2 + (1-x)^2] \log \frac{W^2}{m_q^2} + 8x(1-x) - 1\} \tag{4}$$

where q runs over all quarks and e_q is the electric charge of quark q. The hadronic part is not well known. We can introduce quark densities in the photon $q_i^\gamma(x, Q^2)$ such that (in LO):

$$\begin{aligned} F_2^\gamma(x, Q^2) &= 2x \sum_i e_{q_i}^2 q_i^\gamma(x, Q^2) \\ q_i^\gamma(x, Q^2) &= q^{PL}(x, Q^2) + q_i^{hadr}(x, Q^2) \end{aligned} \tag{5}$$

There exist many parametrisations for the $q_i^\gamma(x, Q^2)$. The two popular parametrisations GRV-LO [6] and SAS-1d [8] are used in this study.

2 Monte Carlo

This study is based on the Monte Carlo generator PHOJET[1)] [10]. Two other Monte Carlo generators HERWIG[2)] [11] and TWOGAM[3)] [12] are used to check the modelling dependence.

PHOJET, based on the Dual Parton Model, assumes that the physical photon state is a superposition of a point-like state and virtual hadronic states having the same quantum numbers $J^{PC} = 1^{--}$ as the photon. The following contributions are included:

- Reggeon and Pomeron exchange (soft process only).
- Hard resolved photon-photon interaction.
- Single direct interaction.
- Double direct interaction.

In order to distinguish the soft and hard processes, a transverse momentum cutoff $p_t^{cut} = 2.5$ GeV to the partons is applied.

TWOGAM includes contributions from:

- Quark Parton Model (QPM).

[1)] PHOJET v1.05c
[2)] HERWIG v5.9
[3)] TWOGAM v1.71

- Vector meson Dominance Model (VDM). The VDM part is generated according [13]:

$$\sigma_{\gamma\gamma}(W_{\gamma\gamma}, Q^2, P^2) = \sum_{i=T,S} F_i(Q^2) \cdot F_i(P^2) \cdot \sigma_{\gamma\gamma}(W_{\gamma\gamma}) \tag{6}$$

where T is the transverse photon and S is the scalar photon. The GVMD form factor [14] is used for the Q^2 and P^2 dependence:

$$\begin{aligned} F_T(Q^2) &= \sum_V r_V \left(\frac{m_V^2}{m_V^2 + Q^2}\right)^2 + r_c \frac{m_0^2}{m_0^2 + Q^2} \\ F_S(Q^2) &= \sum_V \xi \frac{Q^2}{m_V^2} r_V \left(\frac{m_V^2}{m_V^2 + Q^2}\right)^2 \end{aligned} \tag{7}$$

where $V = \rho, \omega, \phi$, $\xi = 0.25$, $r_\rho = 0.65$, $r_\omega = 0.08$, $r_\phi = 0.05$ and $r_c = 1 - r_\rho - r_\omega - r_\phi$. Two different models are used for the $W_{\gamma\gamma}$ spectrum: simple VDM (SVDM) [13]

$$\sigma_{\gamma\gamma}(W_{\gamma\gamma}) = 275 + \frac{300}{W_{\gamma\gamma}} \text{ nb} \tag{8}$$

and Donnachie-Landshoff parametrisation (DL) [15, 16]

$$\sigma_{\gamma\gamma}(W_{\gamma\gamma}) = 173 \cdot (W_{\gamma\gamma}^2)^{0.079} + 519 \cdot (W_{\gamma\gamma}^2)^{-0.4678} \text{ nb} \tag{9}$$

Fig. 2 shows the spectrum of these two different models. The clear difference is seen in the high mass region. If one compares the total cross-section of two different models, the difference is only 3% ($E_{beam} = 91$ GeV and $Q^2 > 1$ GeV^2).

- QCD resolved photon contribution (QCD). This model uses the leading order QCD factorisation. A transverse momentum cutoff p_t^{cut} to the partons is also applied to separate the soft and hard processes.

We use TWOGAM in the following two different sets:

- Set1: QPM + VDM (DL parametrisation) + QCD ($p_t^{cut} = 2.3$ GeV)
- Set2: QPM + VDM (simple VDM) + QCD ($p_t^{cut} = 2.5$ GeV)

TWOGAM had been used in the study of DELPHI [3] with Set2.

Unlike the other Monte Carlos, HERWIG deals with the $e\gamma$ vertex directly. The target photon is generated by EPA. The phase-space for the EPA is controlled by the user-specified parameters. HERWIG had been used in the studies of OPAL [2] and ALEPH [4].

The input parton distribution function for these three Monte Carlos is GRV-LO.

The dominant background sources to the $\gamma^*\gamma \to hadrons$ are $\gamma^*\gamma \to \tau^+\tau^-$ and $Z^\circ \to hadrons$. They are simulated by Vermaseren [17] for $\gamma^*\gamma \to \tau^+\tau^-$ and JETSET [18] for $Z^\circ \to hadrons$. An additional background from $Z^\circ \to \tau^+\tau^-$ is simulated by KORALZ [19].

All Monte Carlo events are passed through a detector simulation using GEANT [20] and GEISHA [21] programs and reconstructed in the same way as the real data.

3 Data Analysis

3.1 Event Selection

Data have been collected with the L3 detector at $\sqrt{s} \simeq 91$ GeV with a total integrated luminosity of 140.34 pb^{-1} from 1991 to 1995. A detailed description of the L3 detector is given in Ref. [22].

The candidate of singly tagged two-photon hadronic events are selected by requiring:

- Tag requirement. A tagged electron is identified as the highest energy bump in the luminosity monitor with $E_{tag} > 35$ GeV and a polar angle $26 < \theta_{tag} < 66$ mrad.
- Anti-tag requirement. The most energetic bump in the luminosity monitor opposite to the identified tagged electron is required to be less than 12 GeV.
- The number of charged particles must be larger than 2. The charged particles are selected by requiring $p_t > 100$ MeV, $DCA < 10$ mm, $hits > 12$ and $hits/span > 0.75$.
- The visible invariant mass W_{vis} of the hadronic final state is required to be in the range $3 \leq W_{vis} \leq 40$ GeV. The clusters of the luminosity monitor, excluding the tagged electron, are assumed to be pions and included in the W_{vis} calculation.
- The transverse momentum component of the hadronic state perpendicular to the tag plane p_t^{out} is required to be less than 5 GeV. The p_t^{bal}, the sum of the transverse momentum of e_{tag} and the transverse momentum component of the hadronic state in the tag plane, has to be smaller than 5 GeV. The tag plane is defined by the beam axis and the tagged electron.

After these cuts, a total of 9928 events are selected in the Q^2 range $1.2 < Q^2 < 9$ GeV^2. The sample is divided into two Q^2 bins: $1.2 < Q^2 < 3$ GeV^2 and $3 < Q^2 < 9$ GeV^2. Table 1 shows the number of selected event and the expected background. The contamination of $Z^\circ \to \tau^+\tau^-$ is negligible.

Q^2(GeV)	selected	$\gamma^*\gamma \to \tau^+\tau^-$	$Z^\circ \to hadrons$
1.2 - 3.0	5772	117.1	35.4
3.0 - 9.0	4156	119.1	84.0

Table 1: The number of selected event in the data, and the expected background contributions from the Monte Carlo, normalised to the data luminosity.

These singly tagged two-photon hadronic events are triggered by the TEC trigger and the single tag trigger. The TEC trigger requires at least two charged particles, each with $p_t > 150$ MeV, back-to-back in the transverse plane within 41°. The single tag trigger requires at least 30 GeV deposited in one luminosity monitor, in coincidence with at least one track in the central part of the detector. The total trigger efficiency is 95.3% (80.5% for the TEC trigger and 76.1% for the single tag trigger). The efficiency of the single tag trigger is lower because it was not operational all the time (29 pb^{-1}). Fig. 3 shows the E_{tag} dependence of trigger efficiency. These dependence has been applied in the Monte Carlo simulation.

To improve the measurement of W_{vis}, we include the kinematics of tagged electron in the visible mass calculation. Assuming that the transverse momentum of the target photon is negligible, we define W_{rec} as [23]:

$$\begin{aligned} W_{rec}^2 &\equiv (p_+^{e_{in}} - p_+^{e_{tag}})(\sum_i p_-^i) - |p_t^{e_{tag}}|^2 \\ p_\pm &\equiv E \pm p_z \end{aligned} \tag{10}$$

where i runs over all hadrons. The comparison of W_{tru}, W_{vis} and W_{rec} is shown in Fig. 4. A significant improvement is seen in using the W_{rec} variable.

To check the contamination of the beam gas and beam wall events, we look at the radius of the secondary vertex, shown in Fig. 5, and the ratio of the positive over negative charged particle, listed in Table. 2. No special structure is seen at the beam wall position (50 mm) and the ratio of the positive over negative charged particle agrees with the Monte Carlo expection.

	N_{ch}^-	N_{ch}^+	N_{ch}^-/N_{ch}^+
data	26052	26494	98.3%
PHOJET	72581	73545	98.7%

Table 2: The ratio of the positive and negative charged particle. The Monte Carlo is unormalised.

3.2 Comparison of the data with the different Monte Carlo generators

Due to the finite detector resolution and the limited detector acceptance, the correlation of $W_{vis}(W_{rec})$ and $W_{\gamma\gamma}$ depends on the modelling of the final state. Therefore the measurement of F_2^γ and the modelling of the final state are strongly connected. To choose the good modelling of the final state, a detailed comparison of the observed final state and the predictions is necessary.

Q^2(GeV^2)	data-bkg	PHOJET	HERWIG	TWO(set1)	TWO(set2)
1.2-3.0	5619.5	5039.3	4767.9	5543.3	5247.1
3.0-9.0	3952.9	3553.6	3938.8	4377.7	4209.4

Table 3: The list of the number of selected event and expection from the different Monte Carlo. TWO(set1) and TWO(set2) indicate TWOGAM with two different sets.

Table. 3 shows the number of selected event and expected event from the different Monte Carlo in two different Q^2 interval. The prediction of PHOJET is about 10% lower than the data. Fig. 6 shows the comparison in the number of charged particle. TWOGAM produces two many low multiplicity events. The p_t of charged particles is shown in Fig. 7. HERWIG disagrees with data in high p_t region. The energy in the electro-magnetic calorimeter and in the hadron calorimeter is shown in Fig. 8 and 9. The agreement is reasonable between data and the different Monte Carlos. The Q^2 and E_{tag} distributions are shown in Fig. 10 and 11. The clear discrepancy between data and Monte Carlos is seen in the E_{tag} distribution. Fig. 12 to 16 shows the comparison of the visible hadronic invariant energy, mass and x, calculated from Eq. 2 and 7. TWOGAM agrees with data well in E_{vis}, W_{vis} and x_{vis}. TWO(set1) is better than TWO(set2) in small x_{vis}. PHOJET shows a good agreement with data in the spectrum of W_{rec} and x_{rec}.

The spectrum of $\Delta\theta = \theta_{hadr} - \theta_{tag}$ and $\Delta\phi = \phi_{hadr} - \phi_{tag}$ are shown in Fig. 17 and 18. The spectrum of p_t^{out} and p_t^{bal} are shown in Fig. 19 and 20. A clear discrepancy between data and HERWIG is shown in these four spectrums. Fig. 21 and 22 show the energy flow versus the pseudorapidity, defined as $\eta = -\ln(\tan(\theta/2))$, in different Q^2 and x_{vis} range. The tagged direction is always in the negative side and the energy of e_{tag} does not show in the plot. The reasonable agreement between data and the different Monte Carlo is shown in large x_{vis}. In low x_{vis}, both TWOGAM and HERWIG deposit too much energy in the forward region but TWOGAM is better than HERWIG in the central region. PHOJET shows a good agreement in the lower x_{vis}.

The χ^2 test is applied in each spectrum, listed in Table 4. The bold text indicates the lowest χ^2. The Monte Carlos are also normalised to the number of selected event to test the agreement in shape. In summary, PHOJET shows a good agreement with data, but the cross-section is about 10% lower. A clear discrepancy between data and HERWIG is seen, especially in the spectrum of the p_t of tracks and the energy flow. TWOGAM gives a reasonable description of data, TWO(set1) is better than TWO(set2) in lower x_{vis} region.

Spectrum	dof	PHOJET	HERWIG	TWO(set1)	TWO(set2)
N_{ch}	12	**127.5 (17.60)**	146.8 (56.00)	325.2 (325.1)	483.7 (476.4)
p_t^{trk}	79	619.1 **(127.3)**	3066. (2375.)	**351.9** (523.9)	768.8 (665.1)
E_{ECAL}	34	**300.0 (148.8)**	324.8 (226.2)	321.5 (324.0)	406.5 (340.0)
E_{HCAL}	42	**322.8 (177.3)**	714.8 (577.8)	365.1 (370.6)	336.9 (330.6)
Q^2	37	153.7 **(39.00)**	264.3 (163.5)	147.2 (141.5)	**131.1** (127.6)
E_{tag}	12	**269.4 (146.7)**	390.4 (282.1)	341.4 (340.6)	349.4 (344.2)
E_{vis}	39	212.1 **(86.00)**	287.2 (193.3)	153.8 (147.2)	**113.9** (111.2)
W_{vis}	32	277.5 (146.9)	288.6 (194.6)	**113.0 (106.0)**	154.5 (151.2)
x_{vis}	46	251.6 **(129.6)**	295.6 (194.0)	**138.7** (131.6)	148.8 (145.7)
W_{rec}	46	**193.5 (72.72)**	560.8 (440.3)	406.1 (408.3)	519.5 (512.4)
x_{rec}	53	**176.9 (59.00)**	570.0 (436.1)	354.3 (358.3)	431.7 (423.6)
$\Delta\theta$	50	256.7 **(134.4)**	362.9 (257.7)	**191.8** (186.1)	138.0 (135.1)
$\Delta\phi$	50	**268.2 (147.9)**	1381. (1214.)	301.7 (298.0)	449.3 (443.0)
p_t^{out}	15	**207.8 (88.70)**	1421. (1275.)	237.6 (231.8)	336.4 (332.1)
p_t^{bal}	15	180.9 **(69.70)**	373.7 (277.5)	**123.3** (114.1)	150.7 (148.2)

Table 4: The list of χ^2 of the different Monte Carlos, normalised to the integrated luminosity and to the number of selected event (number in brackets), calculated in each spectrum. The bold text indicates the best one.

3.3 Unfolding and Extraction of F_2^γ

As we mention and illustrate in Fig. 4, the observed W_{rec} is much smaller than the true two-photon invariant mass W_{tru}. Therefore x_{rec}, calculated from Eq. 2 and 7, is larger than the true x. To extract the x distribution, an unfolding is done in two steps as in Ref. [16].

In order to obtain x from $x_{rec}(x_{vis})$, the following relation is used [24]:

$$
\begin{aligned}
x_{tru}(i) &= \sum_j A_{ij} x_{rec}(j) \\
A_{ij} &= \frac{P(x_{rec}(j)|x(i))P(x(i))}{\sum_l P(X_{rec}(j)|x(l))P(x(l))}
\end{aligned}
\tag{11}
$$

where $P(x_{rec}|x)$ is the likelihood of measuring x_{rec} given a generated x value and $P(x)$ is the generated x distribution after detector acceptance cuts. The matrix A_{ij} is obtained from the Monte Carlo. After the unfolding, the differential cross section in each x interval is calculated by correcting for the detector acceptance (Fig. 23). Fig. 24a shows the differential cross section with $E_{tag} > 35$ GeV, unfolded from PHOJET.

From Eq. 1 and ignoring the y^2 term, the differential cross section is proportional to the F_2^γ [25]:

$$
F_2^\gamma(x, Q^2) = \langle \frac{1}{K(x, Q^2)} \rangle \times \frac{d^2\sigma}{dx dQ^2} \tag{12}
$$

The average correction $\langle \frac{1}{K(x,Q^2)} \rangle$ factor is calculated by the Monte Carlo then applied on the data[4)]. The measured F_2^γ, unfolded from PHOJET, is shown in Fig. 24b and listed in Table. 5. The uncertainty from the limited Monte Carlo statistics is also taken into account. The effect is included by timing the statistical error of the data with a factor of $\sqrt{1+n}$ where $n(= 0.315)$ is the normalisation constant of the Monte Carlo.

3.4 Systematic errors

3.4.1 Uncertainty from the selection

To estimate the uncertainty from the selection, the cuts are varied to:

- $E_{tag} > 37$ GeV.
- $30 < \theta_{tag} < 62$ mrad.
- The number of charged particle has to be larger than 3.
- $p_t^{out} > 10$ GeV and $p_t^{bal} > 10$ GeV.

The four components of the uncertainty from the selection are added in quadrature and listed in Table. 5.

4) The program for the weight calculation is provided by J.H. Field.

Q^2 [GeV^2]	x range	F_2^γ/α	$N_{ch} > 3$	$30 < \theta_{tag} < 62$ [mrad]	$E_{tag} > 37$ [GeV]	p_t^{out} & p_t^{bal} [GeV]
1.9	0.002 - 0.005	0.184 ± 0.009	0.004	~ 0	0.007	0.001
	0.005 - 0.010	0.179 ± 0.007	0.003	0.001	0.003	~ 0
	0.010 - 0.020	0.176 ± 0.006	0.002	0.001	0.002	~ 0
	0.020 - 0.030	0.191 ± 0.008	~ 0	0.002	0.003	0.001
	0.030 - 0.050	0.193 ± 0.008	0.002	0.002	0.005	0.001
	0.050 - 0.100	0.185 ± 0.007	0.006	0.004	0.003	0.001
5.0	0.005 - 0.010	0.307 ± 0.021	0.014	0.006	0.006	0.001
	0.010 - 0.020	0.282 ± 0.014	0.010	0.002	0.003	~ 0
	0.020 - 0.040	0.263 ± 0.011	0.004	0.001	0.003	0.001
	0.040 - 0.060	0.278 ± 0.013	0.003	0.001	0.004	0.001
	0.060 - 0.100	0.270 ± 0.012	~ 0	~ 0	0.003	0.001
	0.100 - 0.200	0.252 ± 0.011	0.004	0.003	0.002	~ 0

Table 5: The list of F_2^γ and the uncertainty from selection cuts in different Q^2 and x bins.

3.4.2 Modelling dependence

To study the modelling dependence of the measured F_2^γ, we unfold the data with HERWIG and TWOGAM(set1). The results from the different Monte Carlo are shown in Fig. 25. The discrepancy in large x is much less than the one in small x. The result from HERWIG is larger than the others. As we discuss in section 3.2, HERWIG disagrees with the data. Therefore the discrepancy from HERWIG is not included in the systematic error. The systematic error only accounts for the discrepancy between PHOJET and TWOGAM.

The OPAL result, unfolded with HERWIG, is also shown in Fig. 25. A good agreement is seen between our result from HERWIG and OPAL.

The unfolding from x_{vis} is also tested. It gives 10% difference in the smallest and largest x points shown in Fig. 26. The error from the Modelling dependence is listed in Table. 6.

3.4.3 P^2 dependence

The mean value of the virtuality of the target photon $\langle P^2 \rangle$, estimated by the Monte Carlo, is 0.07 - 0.08 GeV^2. The behaviour of the P^2 dependence of the F_2^γ is predicted by several theories [7–9]. The non-zero $\langle P^2 \rangle$ effect, estimated by the parameterisation of Schuler and Sjöstrand (SAS-1d), yields to the decrease of F_2^γ by 10 - 20% depend on the x, shown in Fig. 27. Since the distribution of P^2 in the data and the correct theoretical prescription are not known, this uncertainty is not included in the systematic errors.

Fig. 28 show the measured F_2^γ in two different Q^2 bins with the statistical and systematic errors added in quadrature. The results from previous measurements are also shown.

4 Summary

The photon structure photon F_2^γ has been measured at LEP with the L3 detector. The measurement are done at two Q^2 intervals with six x bins from 0.002 to 0.2. The three Monte

Carlo generators PHOJET, TWOGAM and HERWIG are compared with the data. Reasonable agreement is seen with PHOJET and TWOGAM.

Q^2 [GeV^2]	x range	$\langle x \rangle$	F_2^γ/α
1.9	0.002 - 0.005	0.0035	$0.184 \pm 0.009 \pm 0.008^{+0.047}_{-0.010}$
	0.005 - 0.010	0.0075	$0.179 \pm 0.007 \pm 0.004^{+0.020}_{-0.008}$
	0.010 - 0.020	0.015	$0.176 \pm 0.006 \pm 0.003^{+0.015}_{-0.005}$
	0.020 - 0.030	0.025	$0.191 \pm 0.008 \pm 0.004^{+0.002}_{-0.002}$
	0.030 - 0.050	0.040	$0.193 \pm 0.008 \pm 0.006^{+0.007}_{-0.0}$
	0.050 - 0.100	0.075	$0.185 \pm 0.007 \pm 0.008^{+0.025}_{-0.0}$
5.0	0.005 - 0.010	0.0075	$0.307 \pm 0.021 \pm 0.016^{+0.087}_{-0.031}$
	0.010 - 0.020	0.015	$0.282 \pm 0.014 \pm 0.011^{+0.036}_{-0.025}$
	0.020 - 0.040	0.030	$0.263 \pm 0.011 \pm 0.005^{+0.014}_{-0.014}$
	0.040 - 0.060	0.050	$0.278 \pm 0.013 \pm 0.005^{+0.001}_{-0.005}$
	0.060 - 0.100	0.080	$0.270 \pm 0.012 \pm 0.003^{+0.009}_{-0.0}$
	0.100 - 0.200	0.150	$0.252 \pm 0.011 \pm 0.005^{+0.045}_{-0.0}$

Table 6: The measured F_2^γ as a function of x in two Q^2 bins. The $\langle x \rangle$ is the centre of x bin. The first error is statistical. The second error is the error from the selection and the third error from the the modelling dependence.

References

[1] PLUTO Coll., C. Berger et al., Phys. Lett. B 142 (1984) 111;
TASSO Coll., M. Althoff et al., Z. Phys. C 31 (1986) 527;
TPC/2γ Coll., H. Aihara et al., Z. Phys. C 34 (1987) 1;
TOPAZ Coll. K. Muramatsu et al., Phys. Lett. B 332 (1994) 477.

[2] OPAL Coll., K. Ackerstaff et al., Z. Phys. C 74 (1997) 33;
OPAL Coll., K. Ackerstaff et al., CERN-PPE/97-087 (1997);
OPAL Coll., K. Ackerstaff et al., CERN-PPE/97-103 (1997).

[3] DELPHI Coll., P. Abreu et al., Z. Phys. C 62 (1994) 357;
DELPHI Coll., P. Abreu et al., Phys. Lett. B 348 (1995) 665.

[4] ALEPH Coll., Lepton-Photon conference (1997).

[5] V. M. Budenv et al., Phys. Rep. 15 (1975) 181.

[6] M. Glück et al., Phys. Rev. D 45 (1992) 1973;
M. Glück et al., Phys. Rev. D 46 (1992) 13986.

[7] M. Glück et al., Phys. Rev. D 51 (1995) 3220;
M. Glück et al., Phys. Rev. D 54 (1996) 5515.

[8] G. A. Schuler and T. Sjöstrand, Phys. Lett. B 376 (1996) 193.

[9] M. Drees and R. M. Godbole, Phys. Rev. D 50 (1994) 3124.

[10] R. Engel, Z. Phys. C 66 (1995) 203;
R. Engel and J. Ranft, Phys. Rev. D 54 (1996) 4246.

[11] G. Marchesini et al., Comp. Phys. Comm. 67 (1992) 465.

[12] S. Nova et al., DELPHI Note 90-35 (1990).

[13] I. F. Ginzburg and V. G. Serbo, Phys. Lett. B 109 (1982) 231.

[14] J.J. Sakurai and D. Schildknecht, Phys. Lett. B 41 (1972) 489.

[15] A. Donnachie and P. V. Landshoff, Phys. Lett. B 296 (1992) 227.

[16] L3 Coll., M. Acciarri et al., CERN-PPE/97-48 (1997).

[17] J. A. M. Vermaseren, Nucl. Phys. B 229 (1983) 347;
J. A. M. Vermaseren et al., Phys. Rev. D 19 (1979) 137.

[18] T. Sjöstrand, Comp. Phys. Comm. 82 (1994) 74.

[19] S. Jadach, Comp. Phys. Comm. 79 (1994) 503.

[20] R. Brun et al., GEANT 3.15 preprint CERN DD/EE/84-1 (Revised 1987).

[21] H. Fesefeldt, RWTH Aachen report PITHA 85/2 (1985).

[22] L3 Coll., B. Adeva et al., Nucl. Inst. Meth. A289 (1990) 35;
J.A. Bakken et al., Nucl. Inst. Meth. A275 (1989) 81;
O. Adriani et al., Nucl. Inst. Meth. A302 (1991) 53;
B. Adeva et al., Nucl. Inst. Meth. A323 (1992) 109;
K. Deiters et al., Nucl. Inst. Meth. A323 (1992) 162;
M. Chemarin et al., Nucl. Inst. Meth. A349 (1994) 345;
M. Acciarri et al., Nucl. Inst. Meth. A351 (1994) 300;
G. Basti et al., Nucl. Inst. Meth. A374 (1996) 293;
A. Adam et al., Nucl. Inst. Meth. A383 (1996) 342.

[23] Physics at LEP2, CERN 96-01.

[24] G. D'Agostini, Nucl. Inst. Meth. A 372 (1996) 469.

[25] G. F. Susinno, L3 note 2115 (1997).

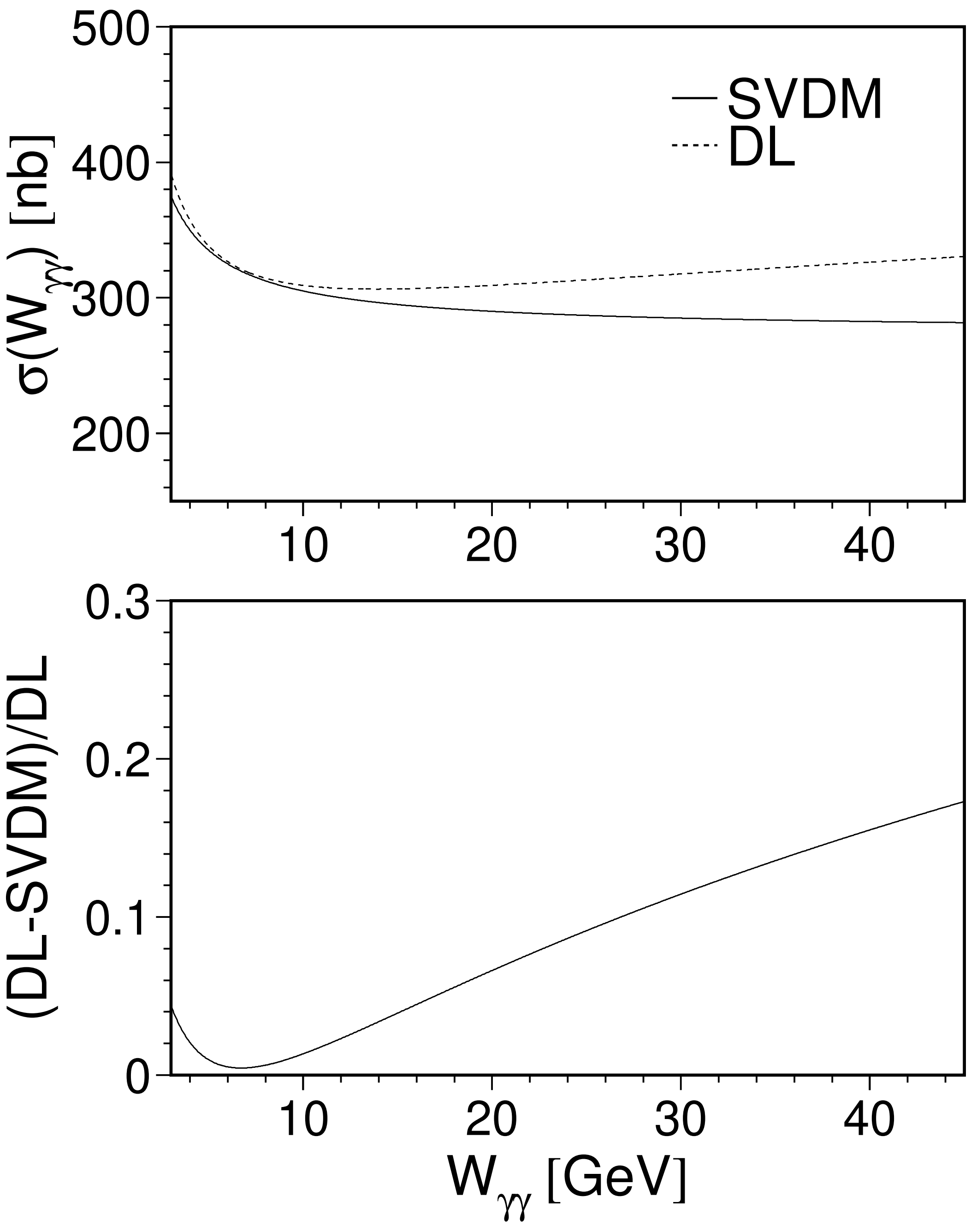

Figure 2: The comparison of different VDM model: simple VDM (SVDM) and Donnachie-Landshoff parametrisation (DL).

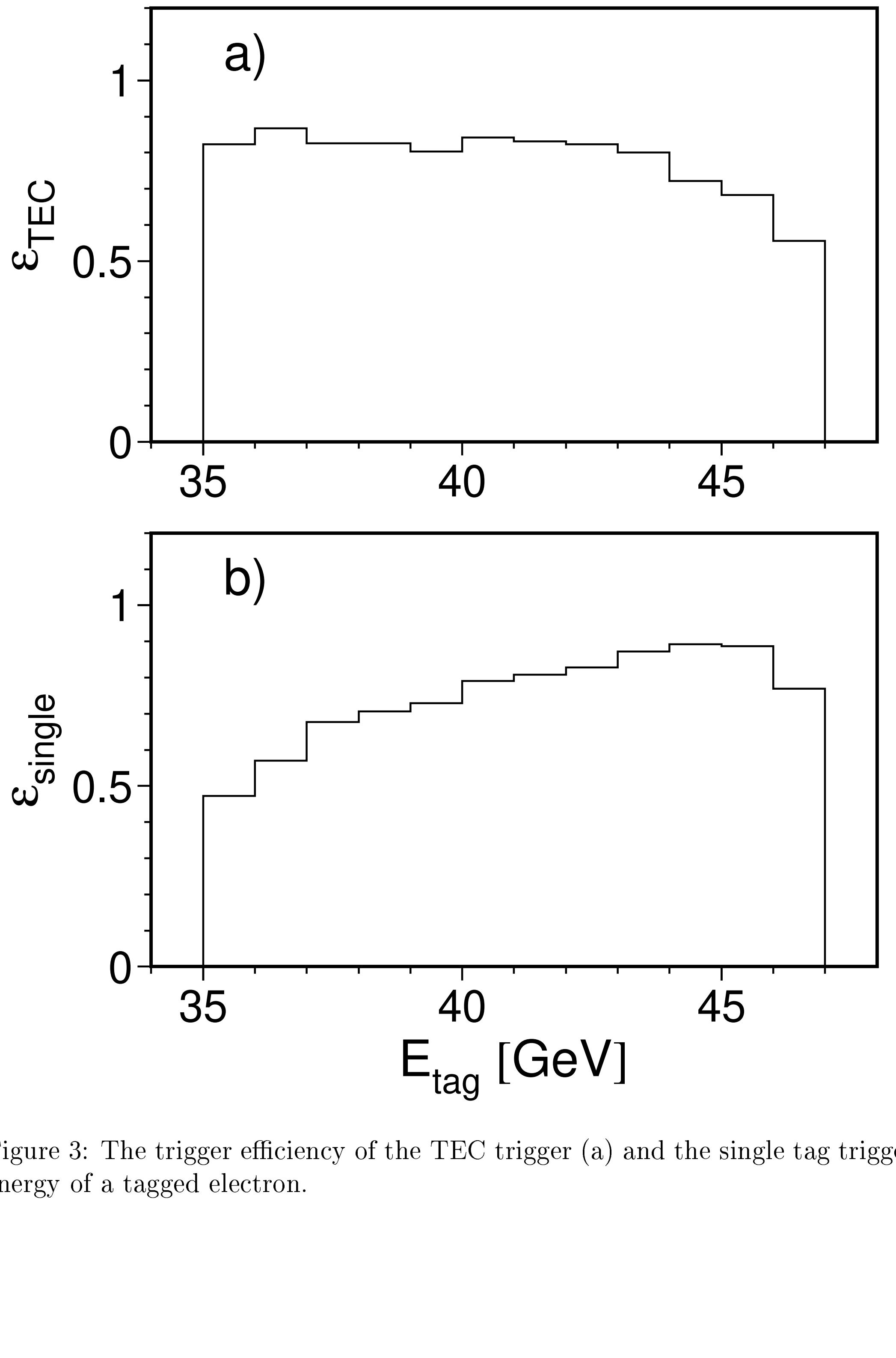

Figure 3: The trigger efficiency of the TEC trigger (a) and the single tag trigger (b) versus the energy of a tagged electron.

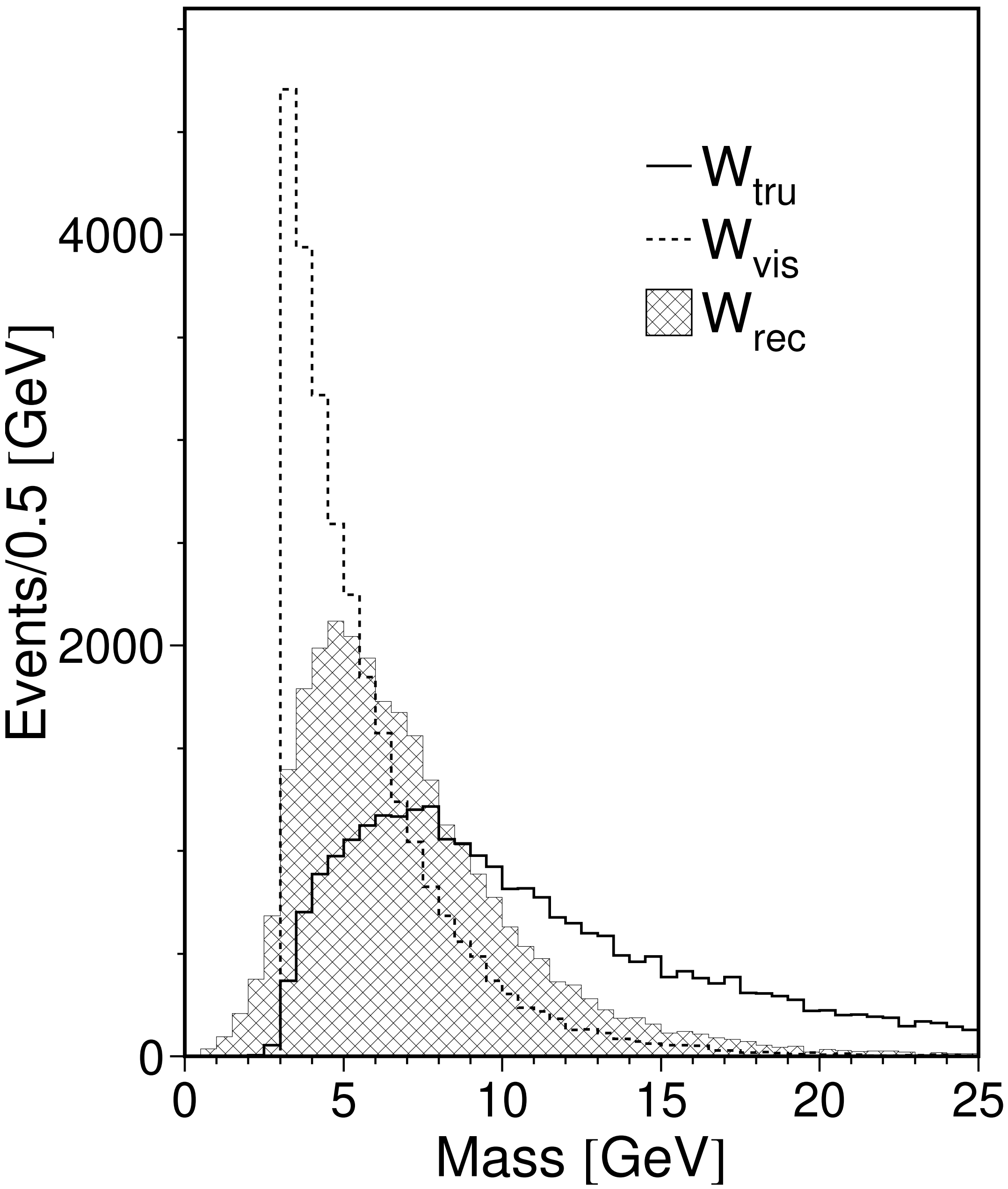

Figure 4: The comparison of W_{tru}, W_{vis} and W_{rec}.

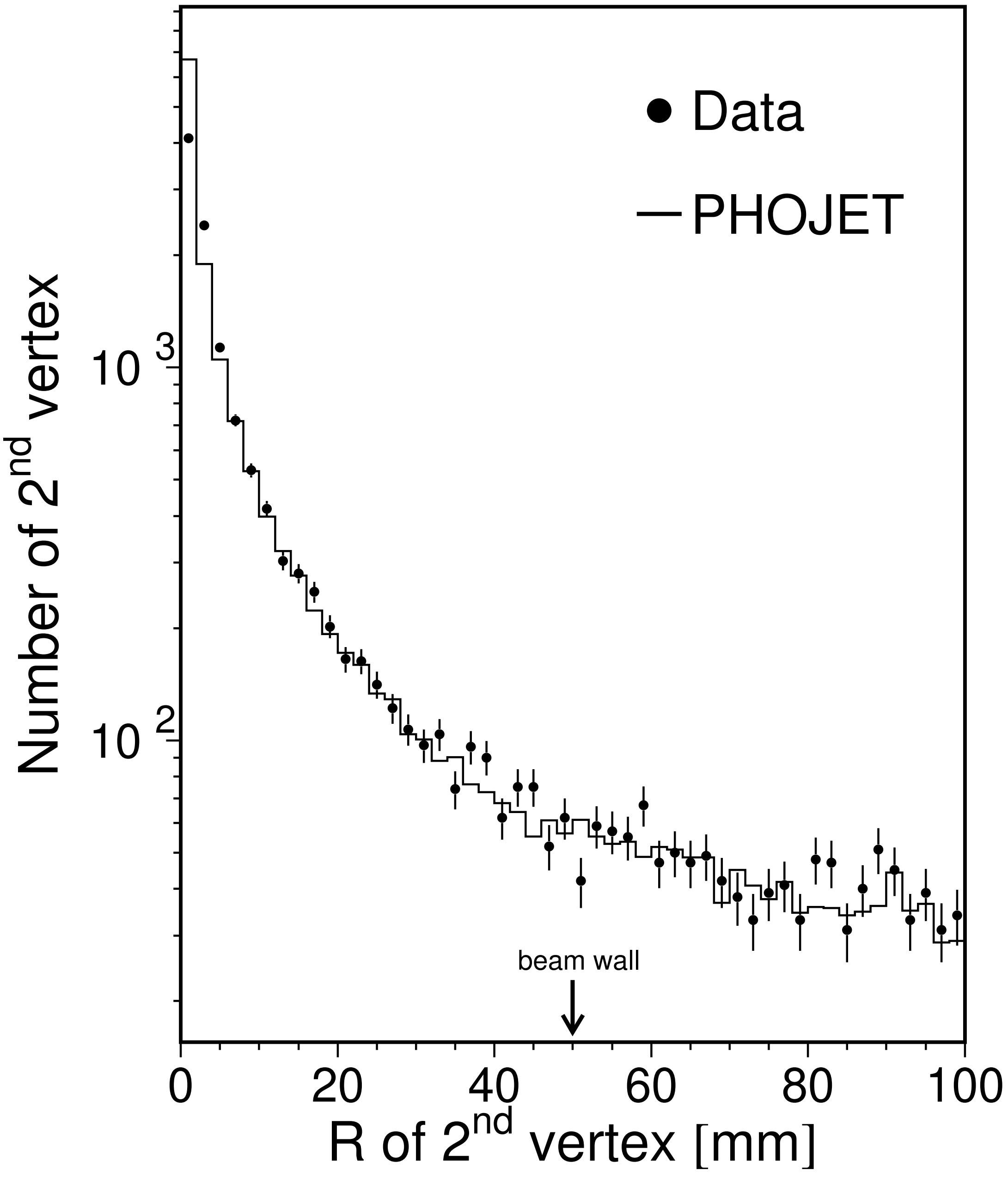

Figure 5: The distribution of the radius of second vertex. The beam wall structure is not seen.

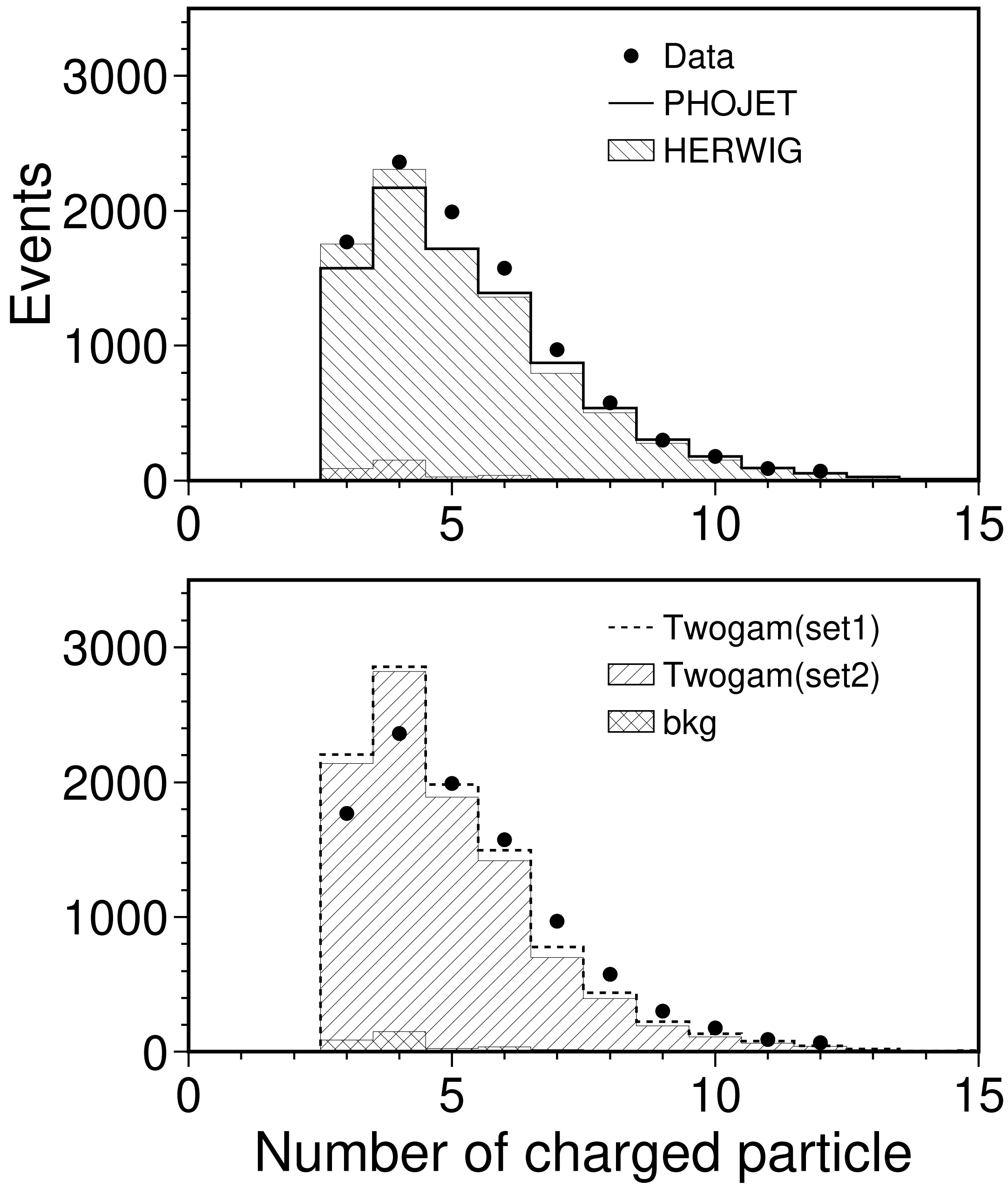

Figure 6: The comparison of the number of charged particle.

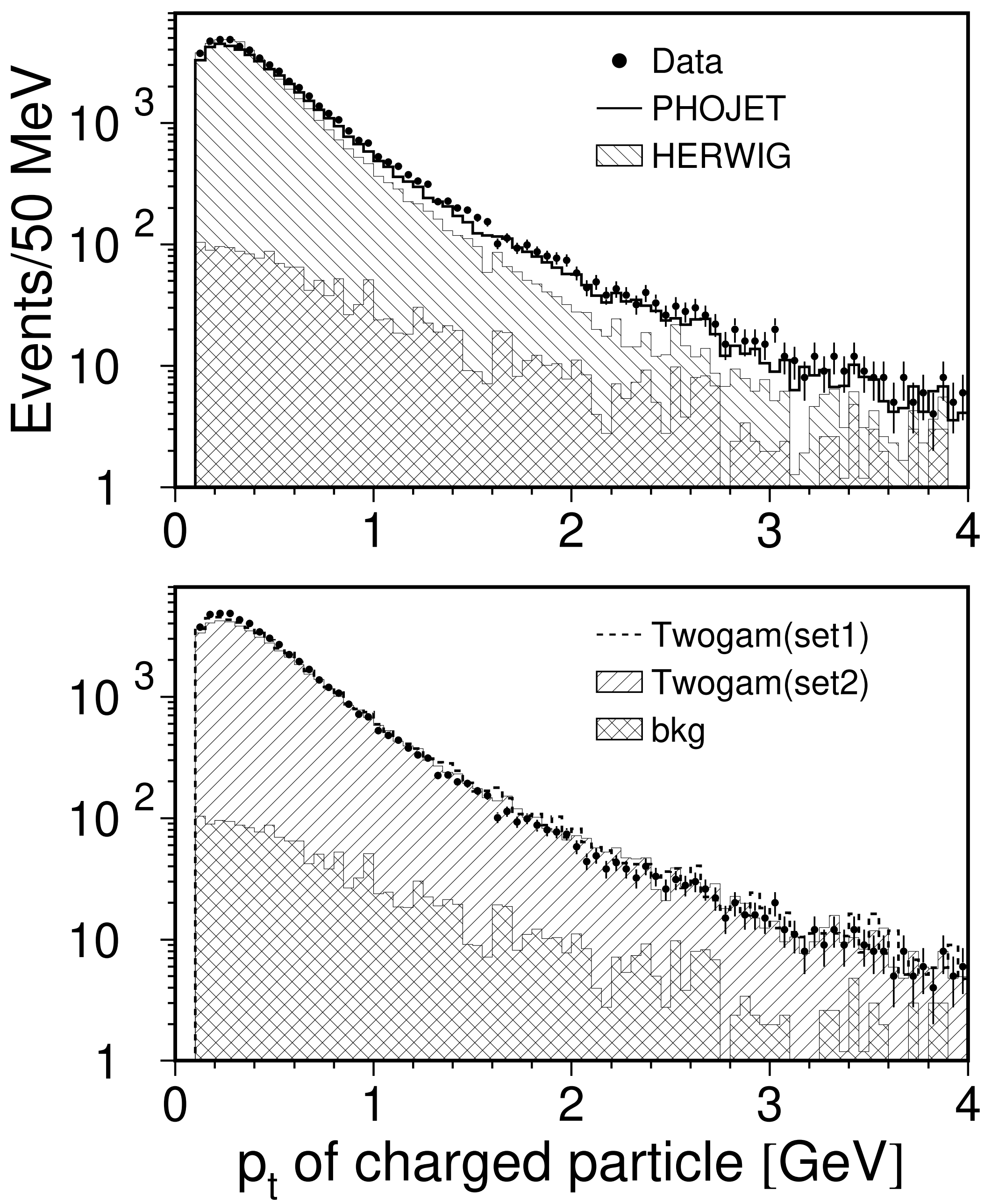

Figure 7: The comparison of the p_t of charged particle.

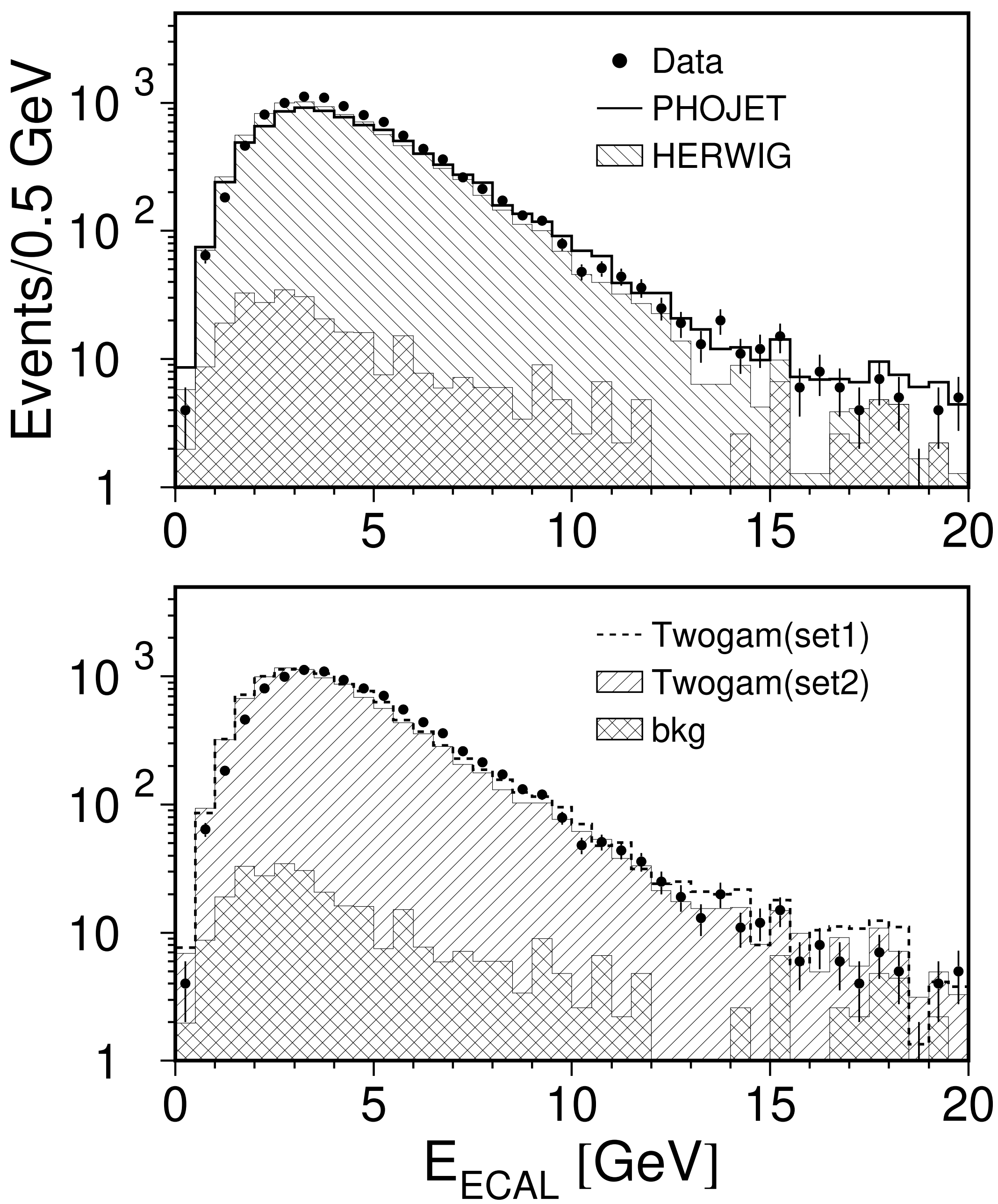

Figure 8: The comparison of the E_{ECAL}.

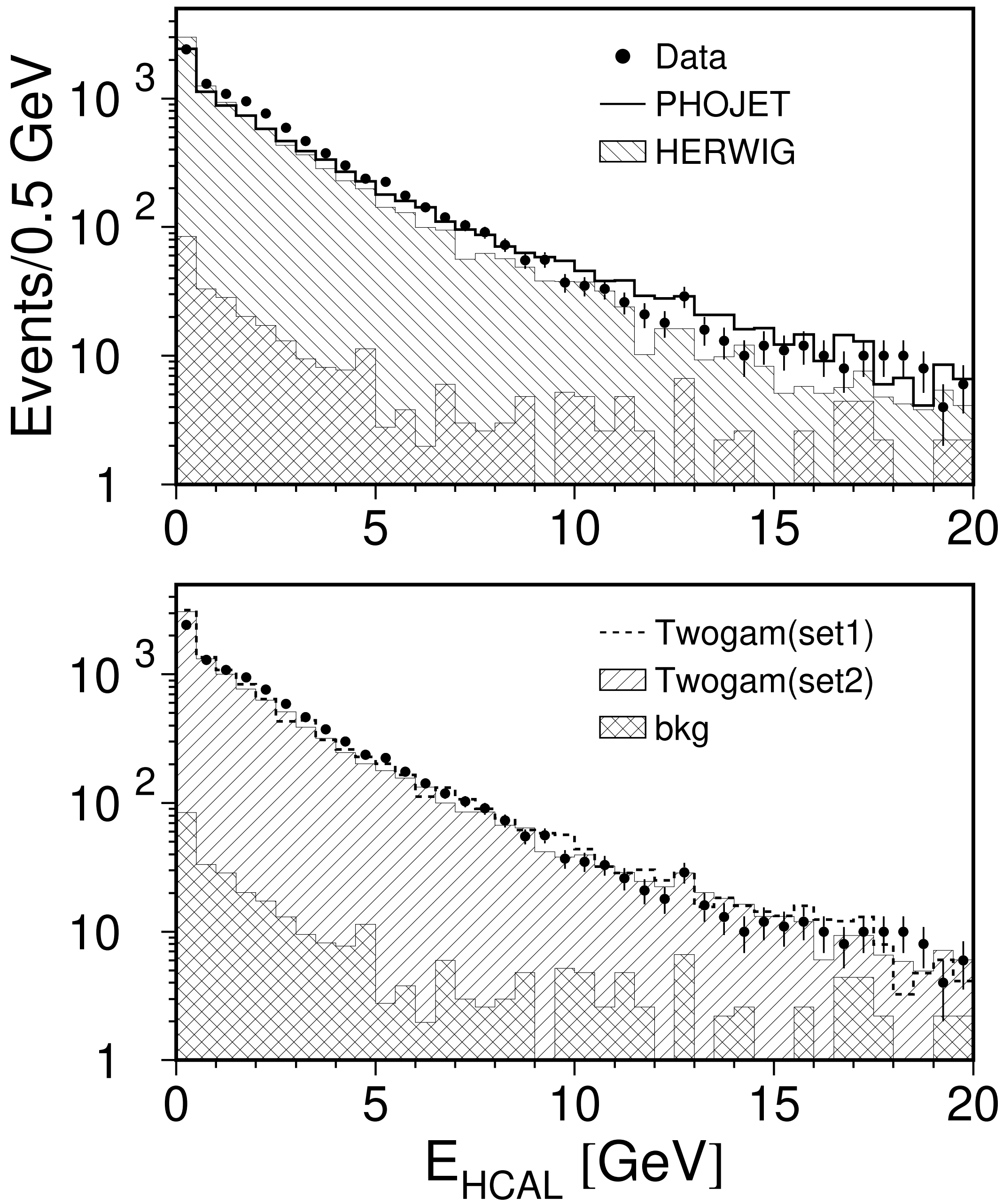

Figure 9: The comparison of the E_{HCAL}.

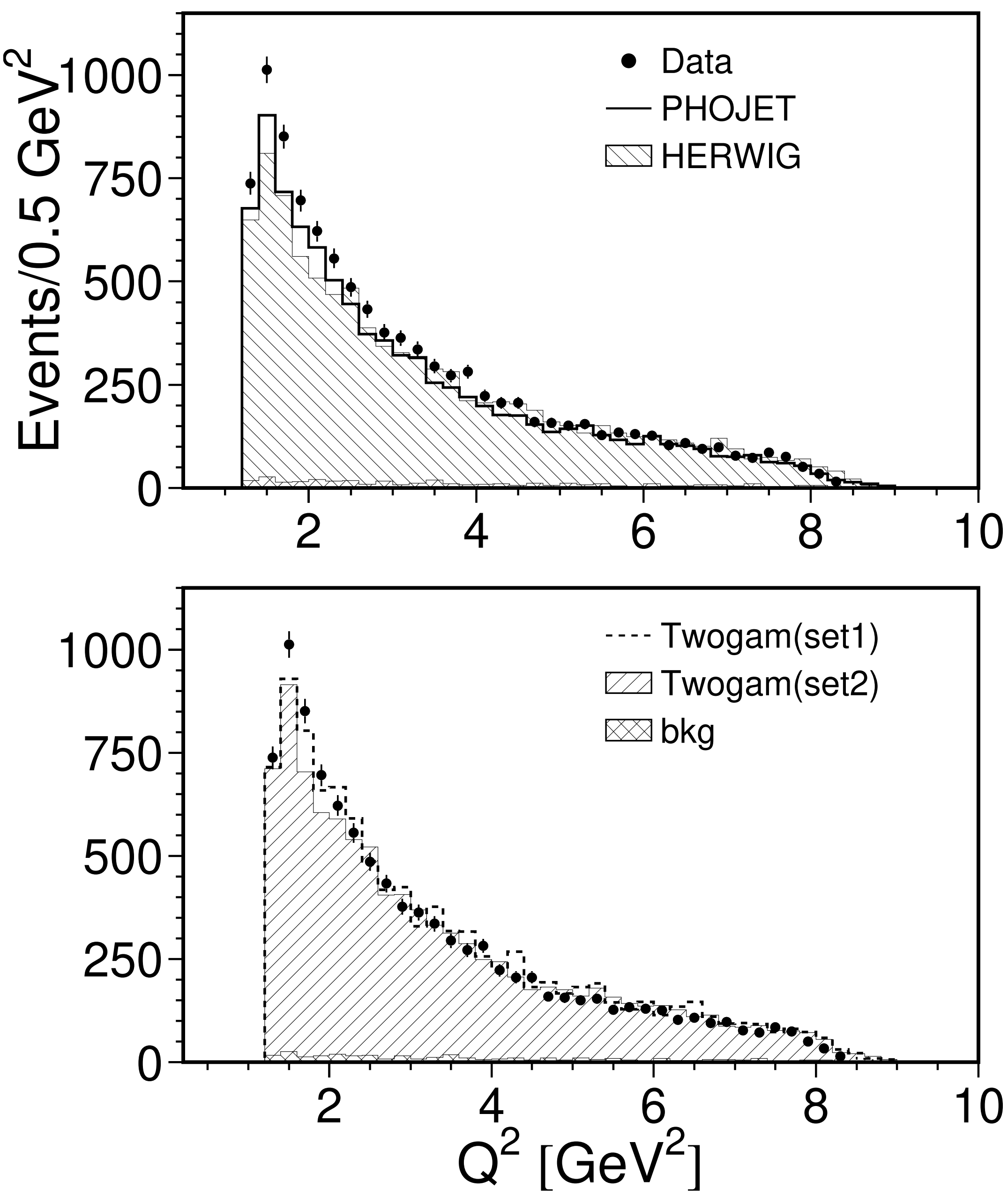

Figure 10: The comparison of the Q^2.

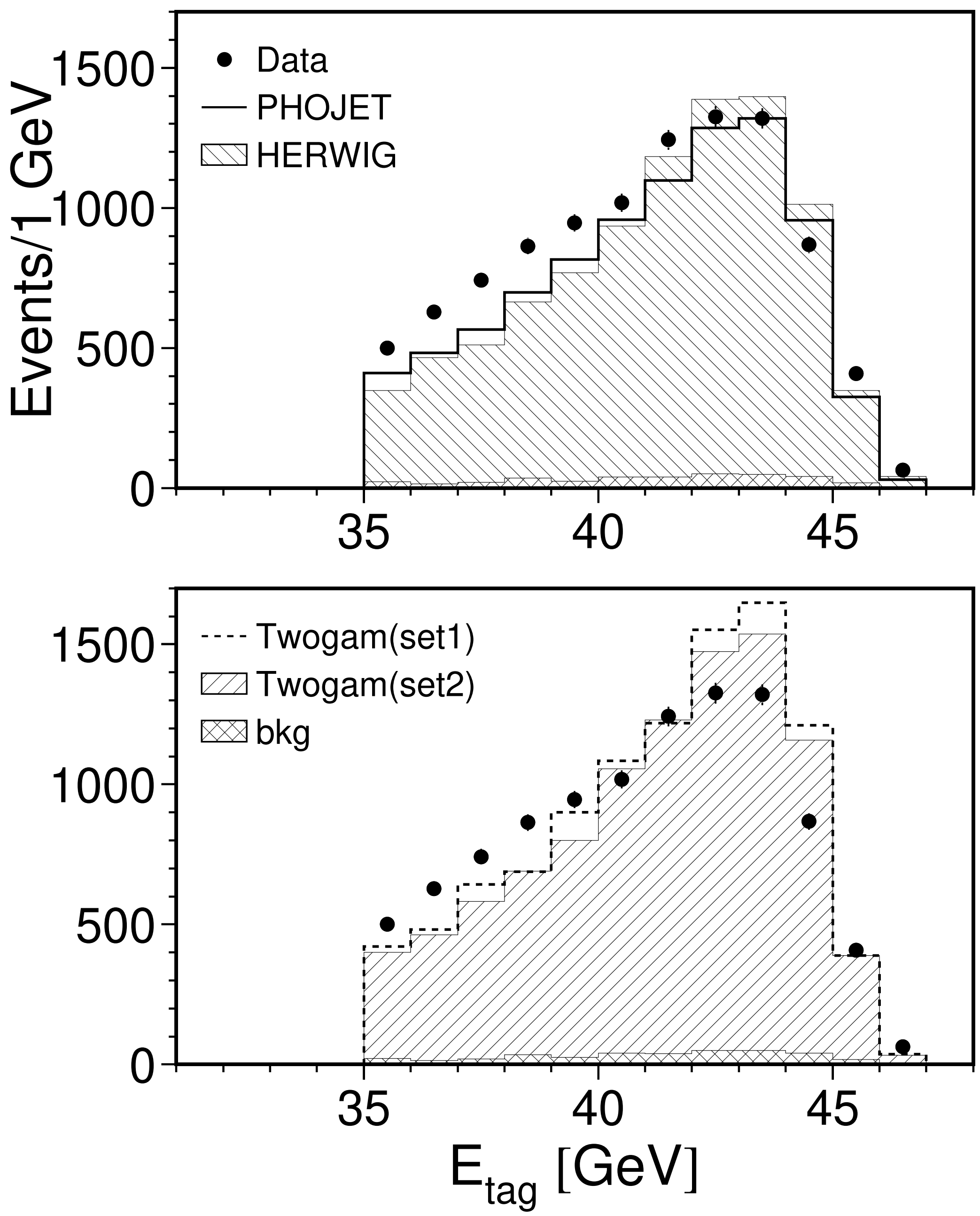

Figure 11: The comparison of the E_{tag}.

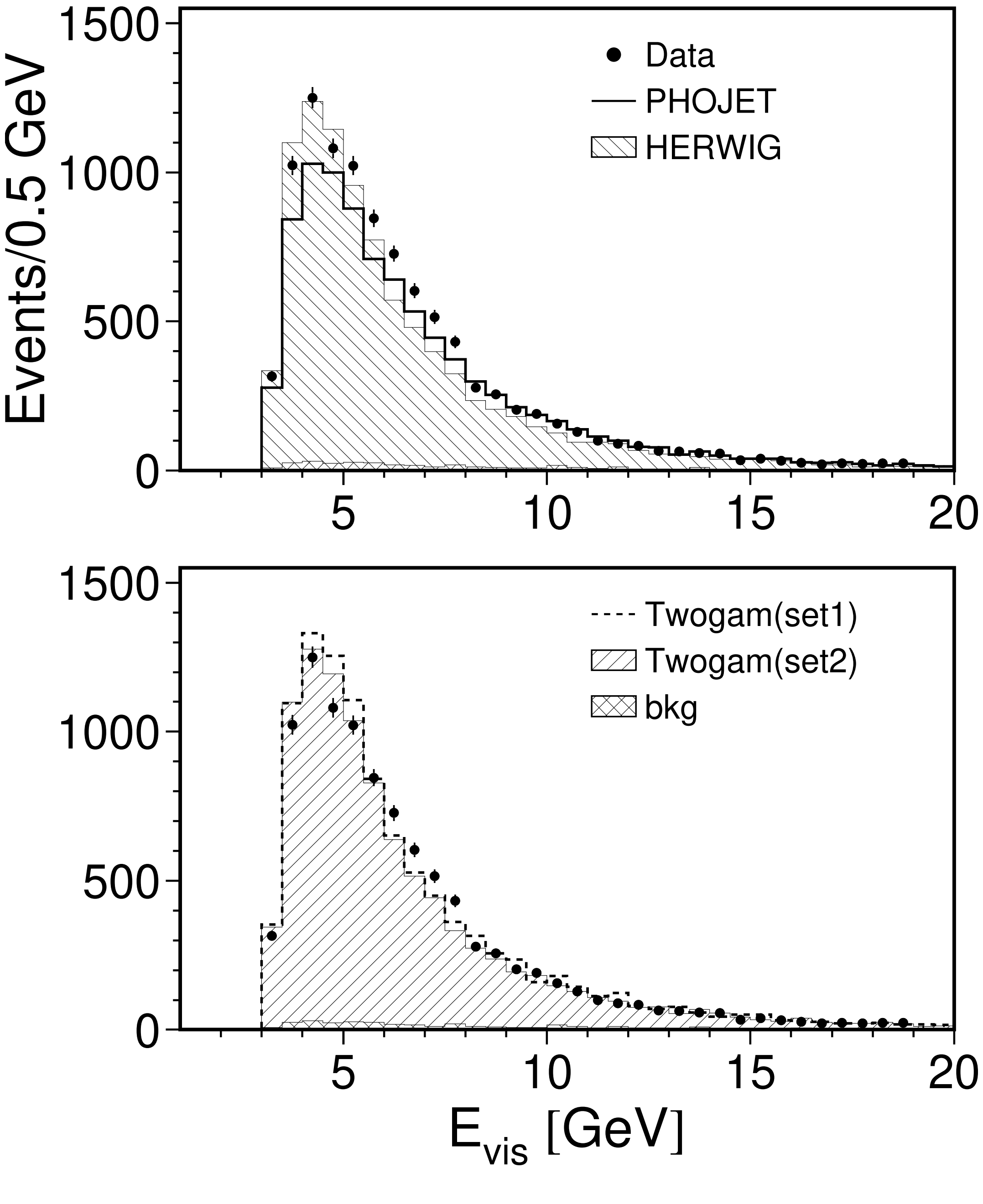

Figure 12: The comparison of the E_{vis}.

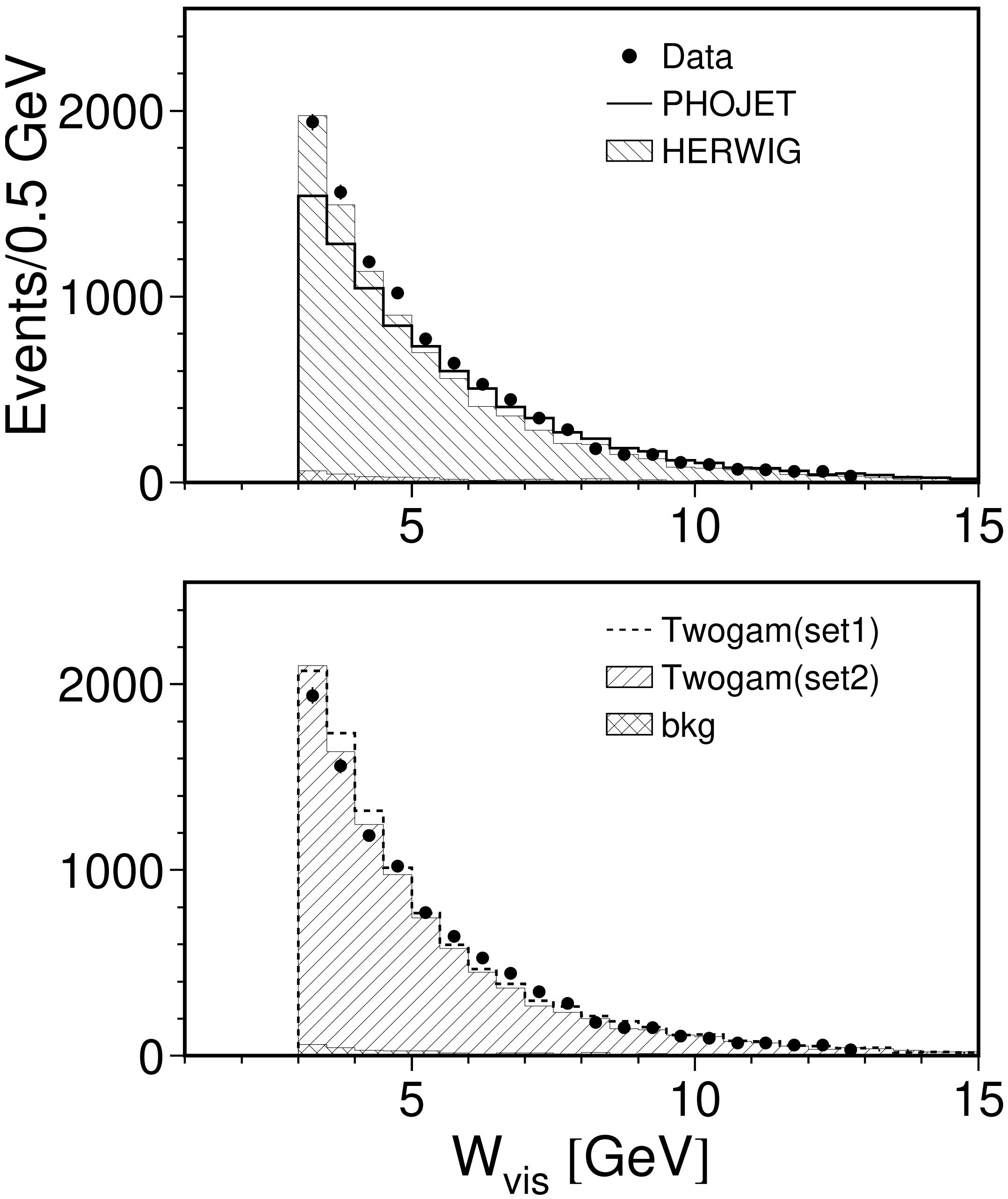

Figure 13: The comparison of the W_{vis}.

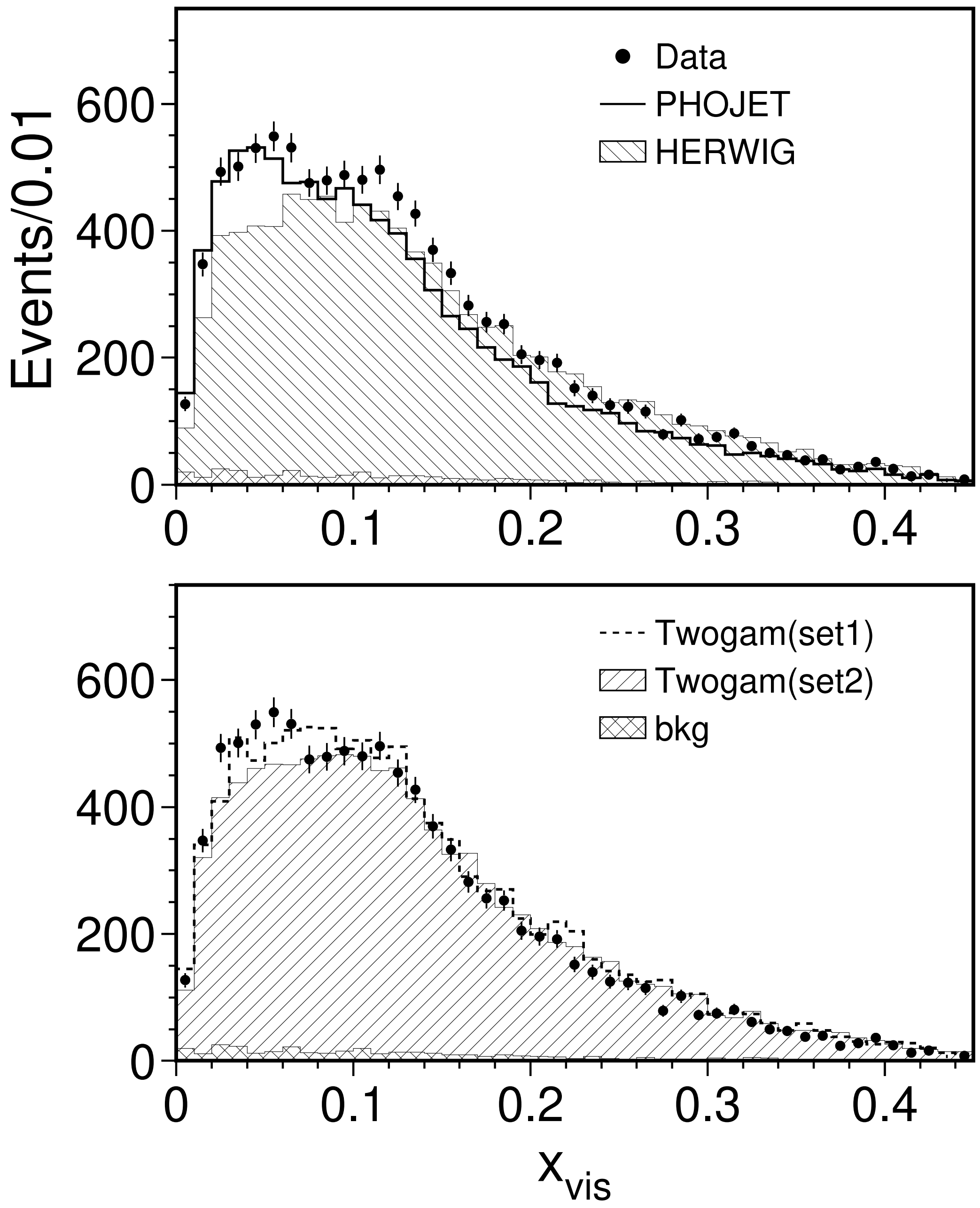

Figure 14: The comparison of the x_{vis}.

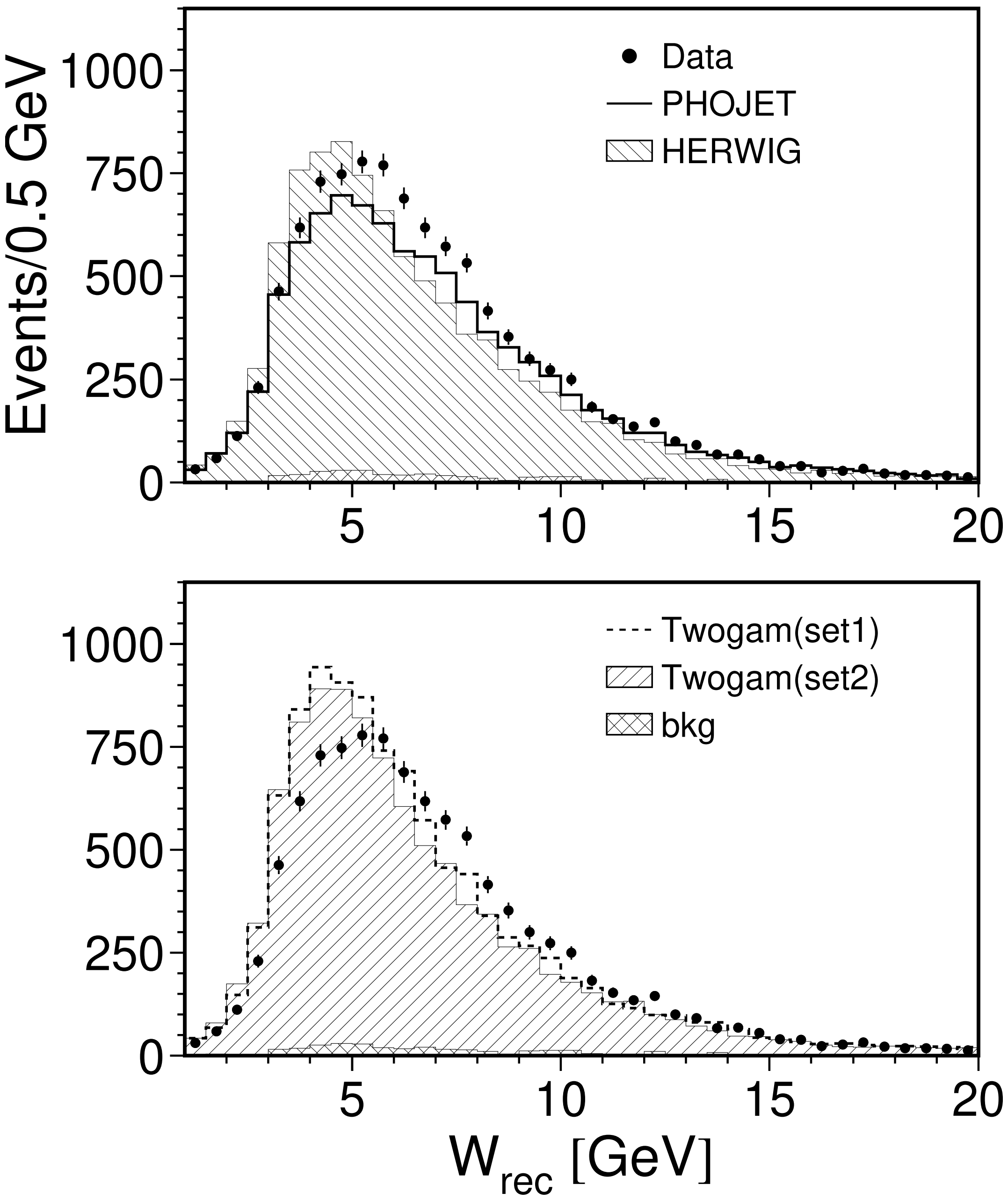

Figure 15: The comparison of the W_{rec}.

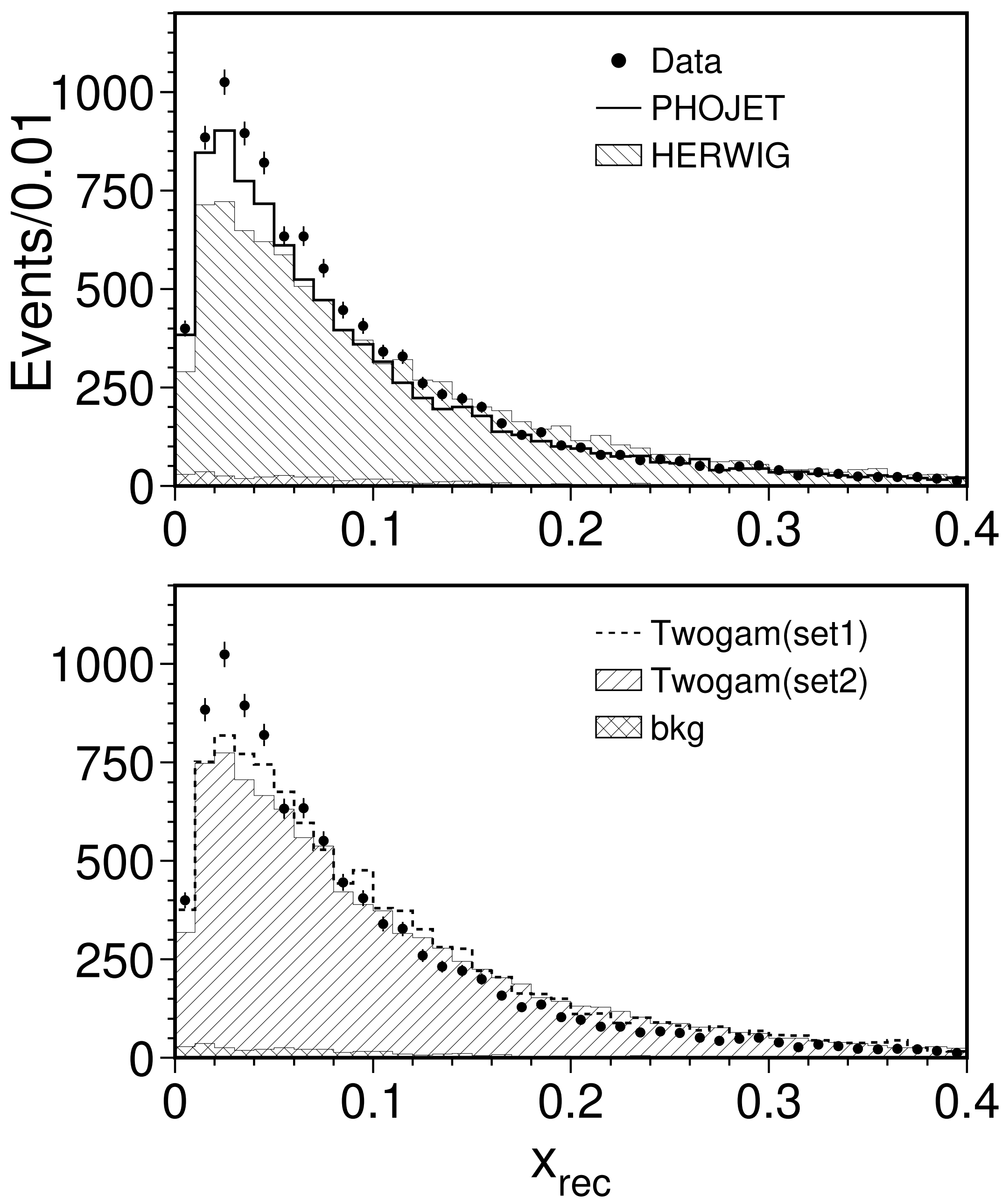

Figure 16: The comparison of the x_{rec}.

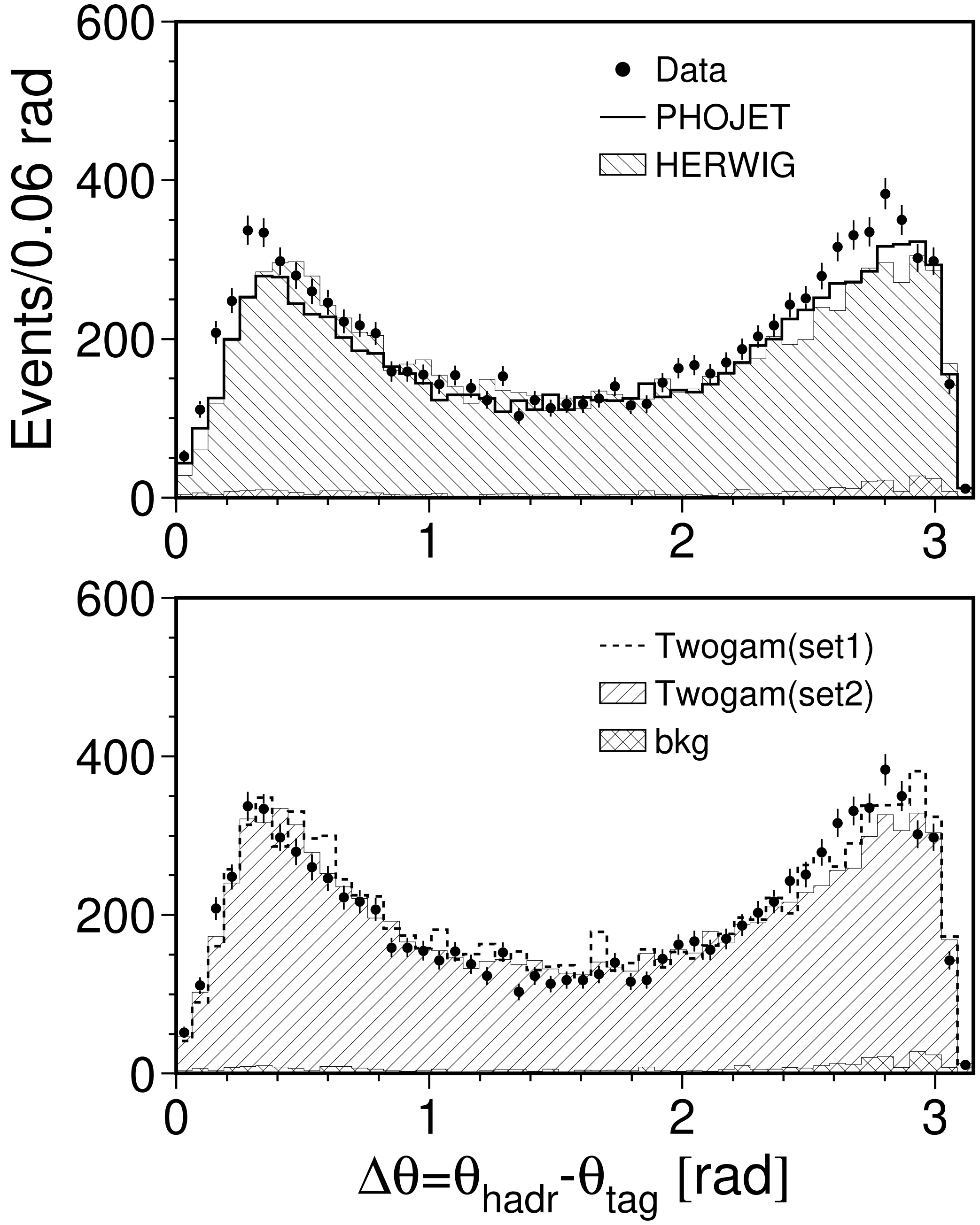

Figure 17: The comparison of the $\Delta\theta = \theta_{hadr} - \theta_{tag}$.

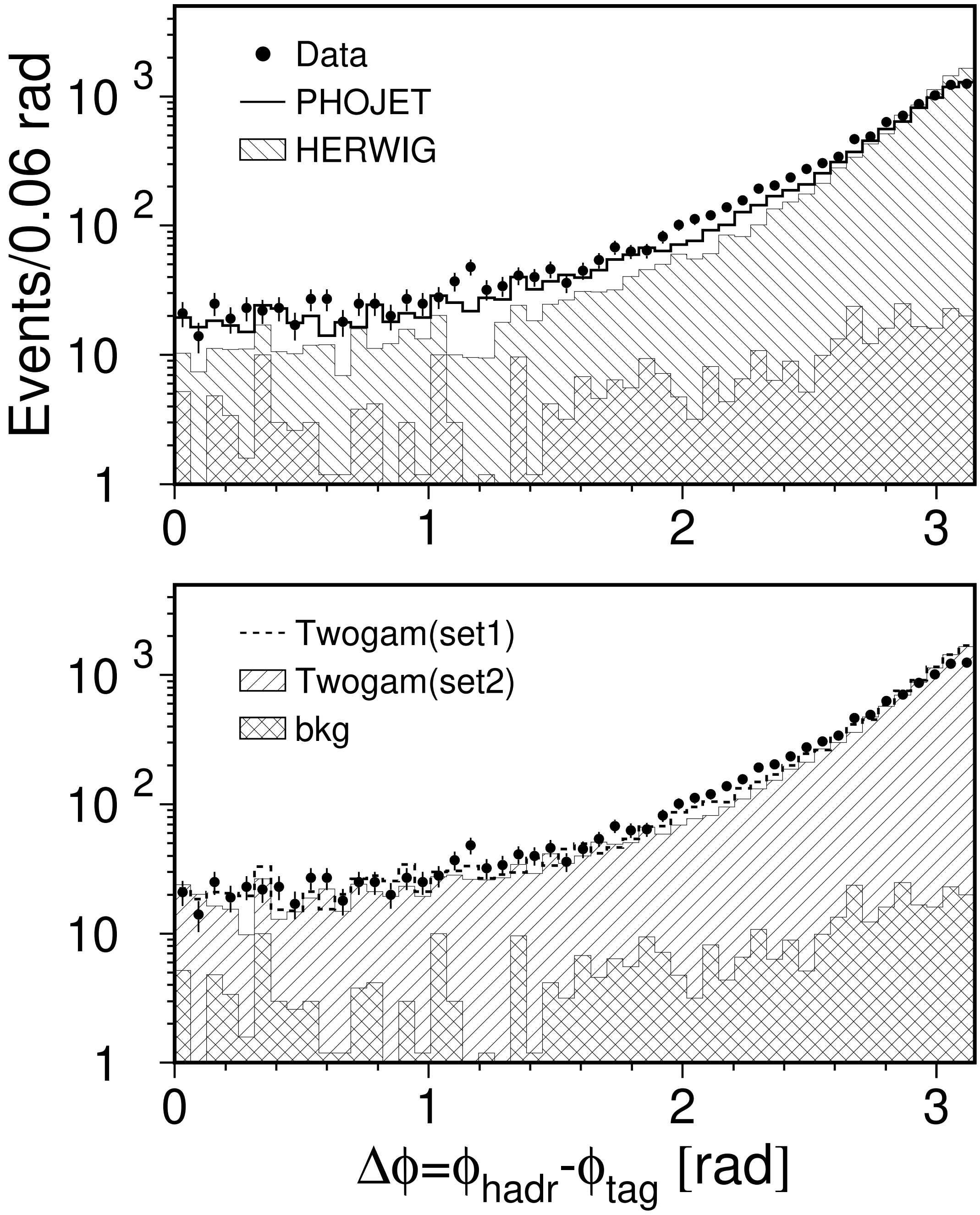

Figure 18: The comparison of the $\Delta\phi = \phi_{hadr} - \phi_{tag}$.

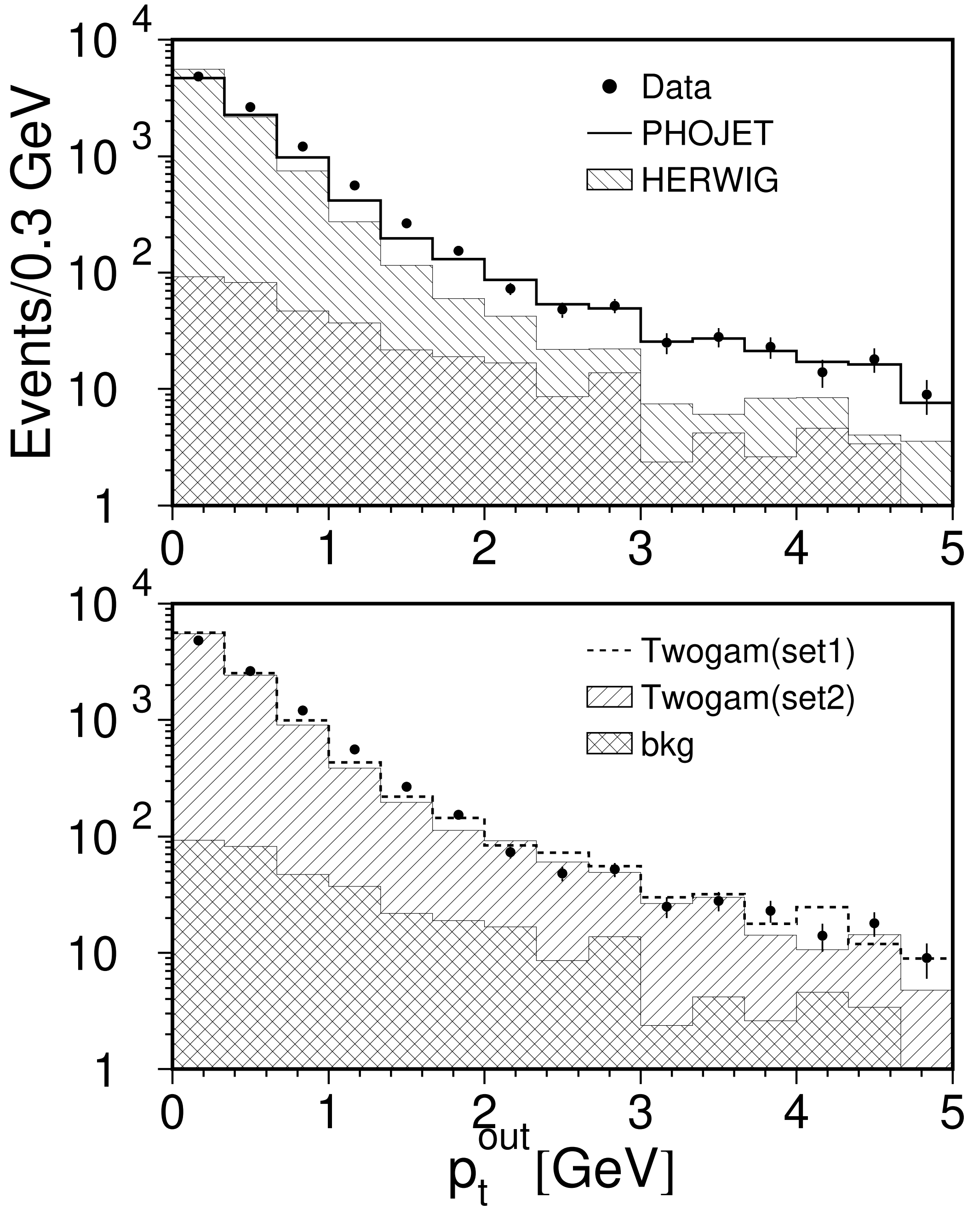

Figure 19: The comparison of the p_t^{out}.

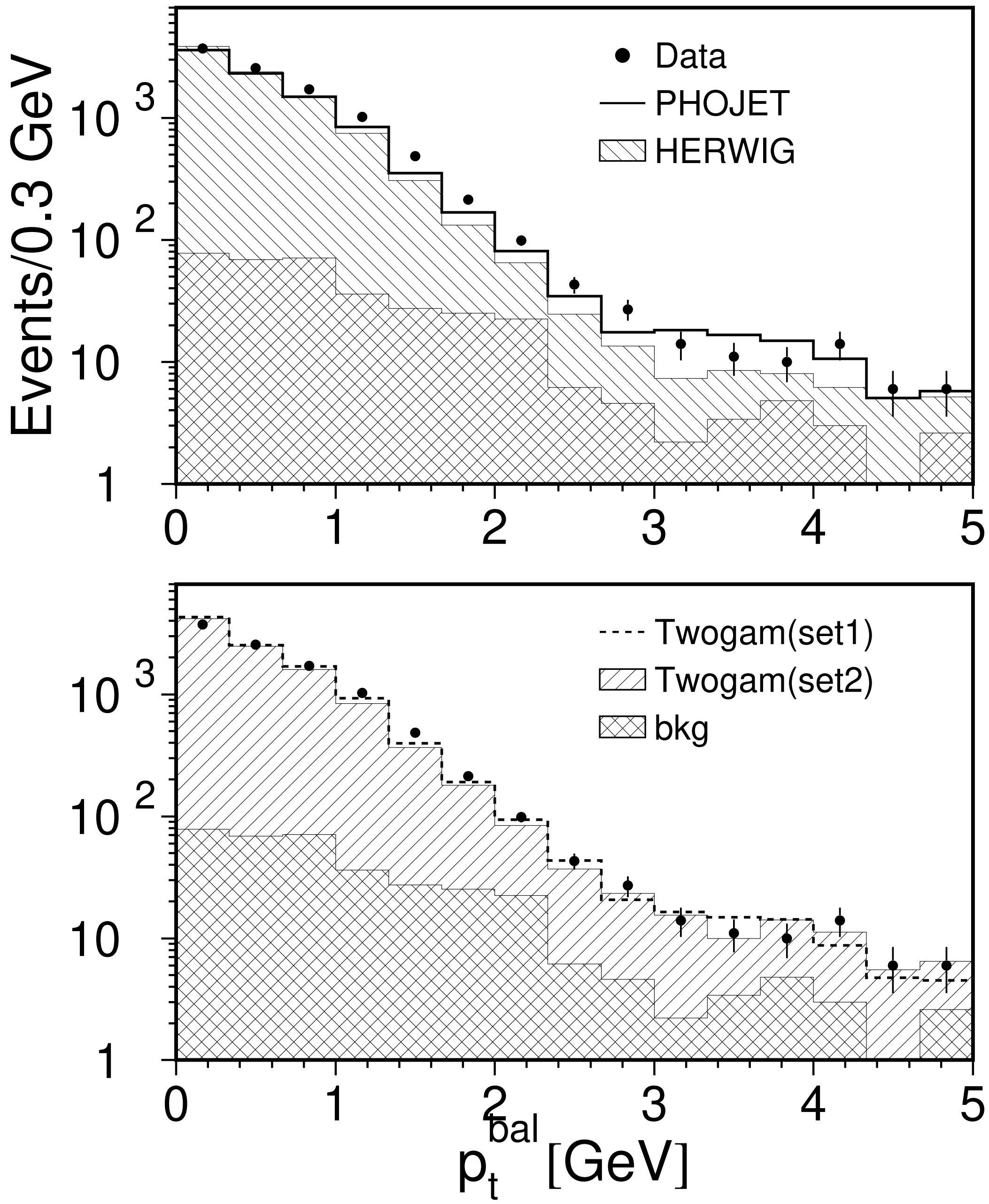

Figure 20: The comparison of the p_t^{bal}.

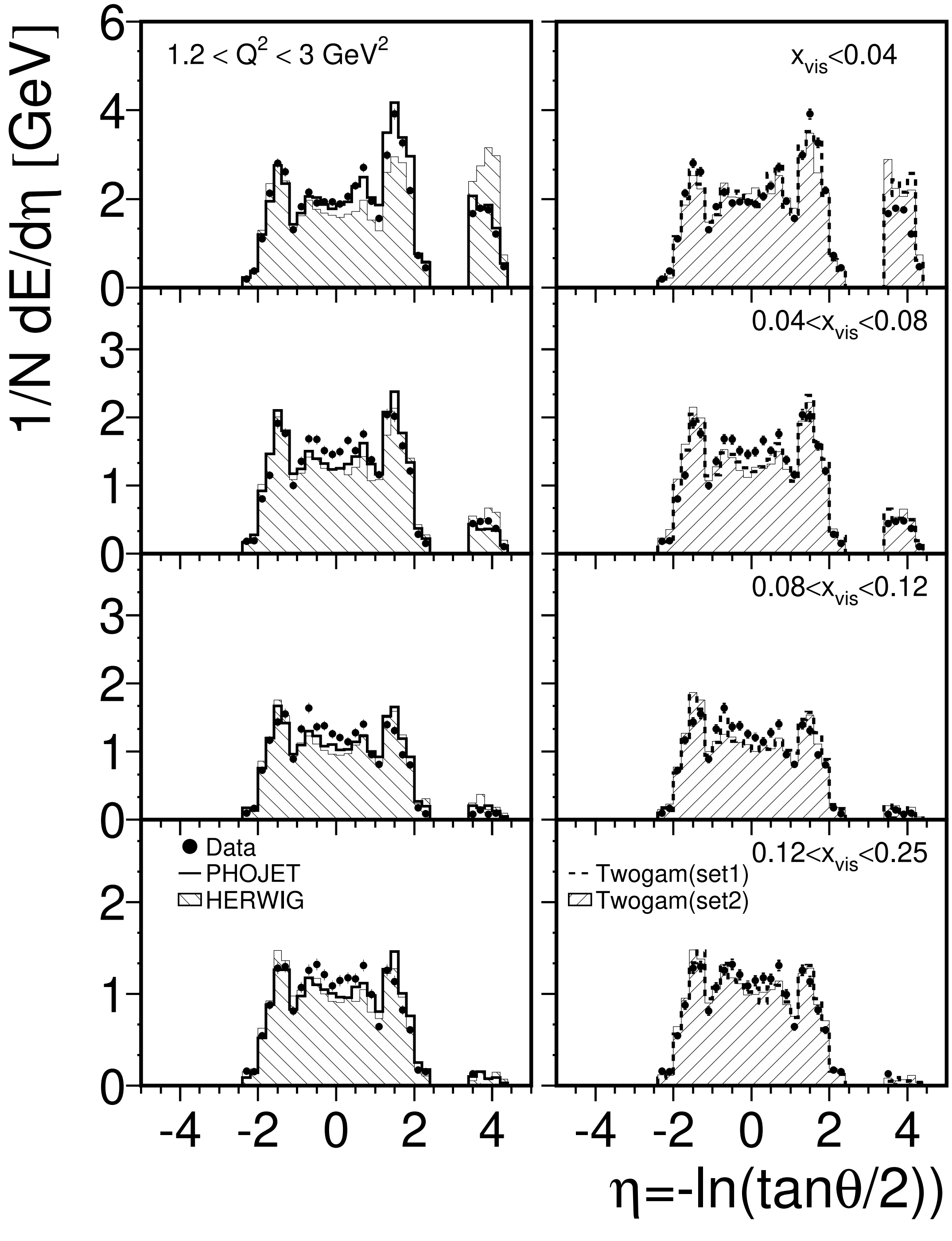

Figure 21: The comparison of the hadronic energy flow in $1.2 < Q^2 3$ GeV^2.

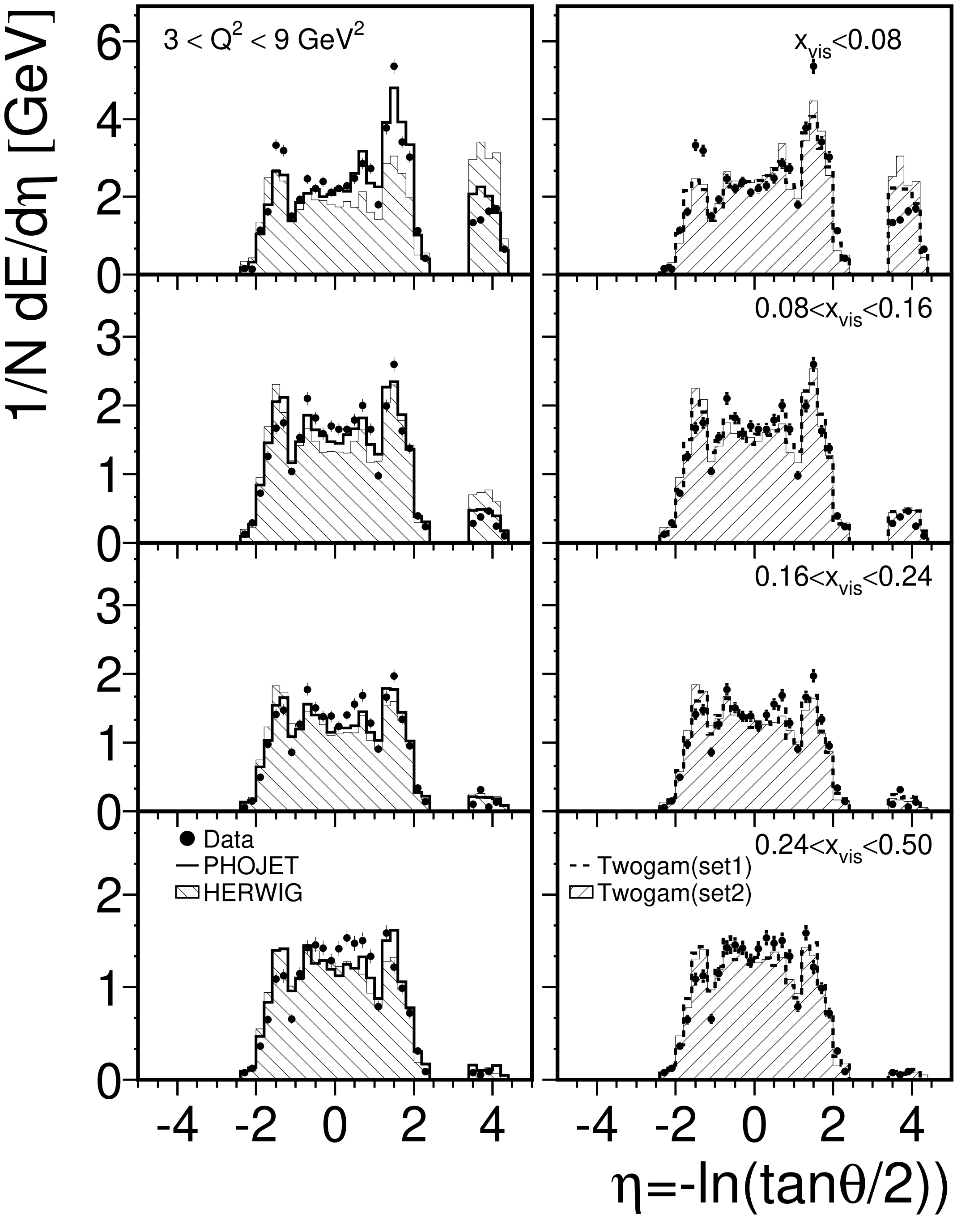

Figure 22: The comparison of the hadronic energy flow in $3 < Q^2 9$ GeV^2.

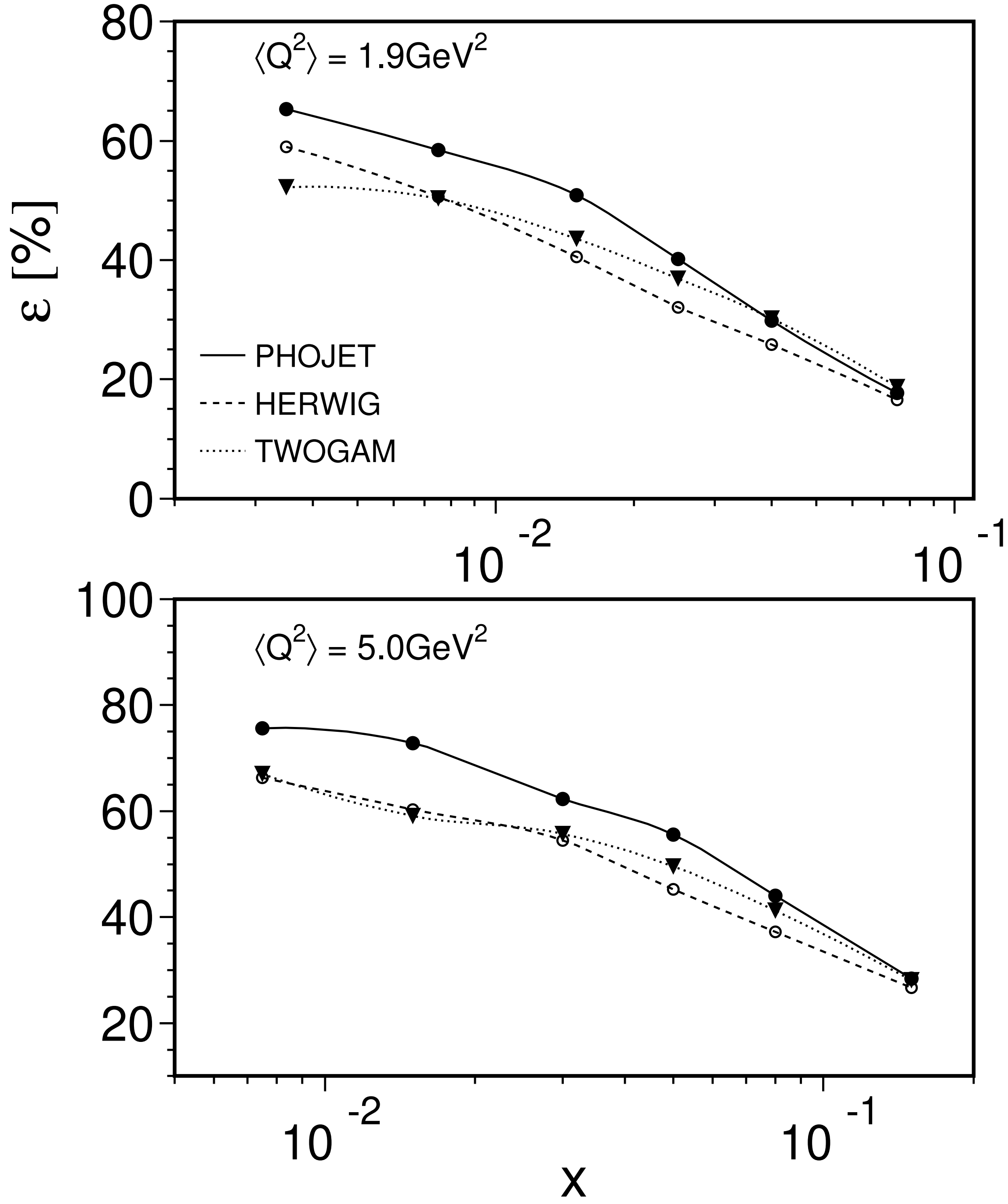

Figure 23: The detector acceptance estimated by th different Monte Carlos.

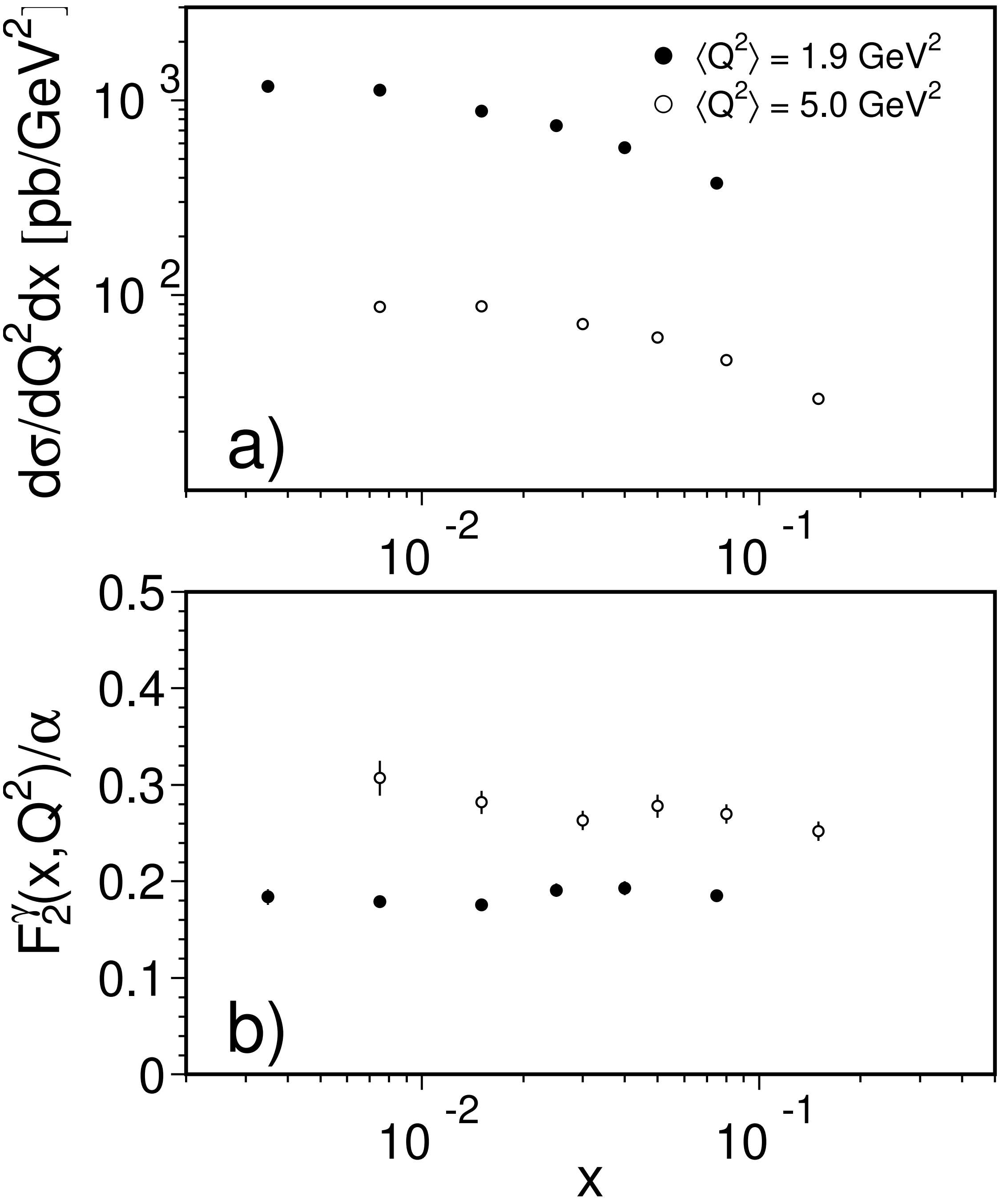

Figure 24: The result unfolded by the PHOJET. a) The differential cross-section with $E_{tag} >$ 35 GeV. b) The photon structure function F_2^γ.

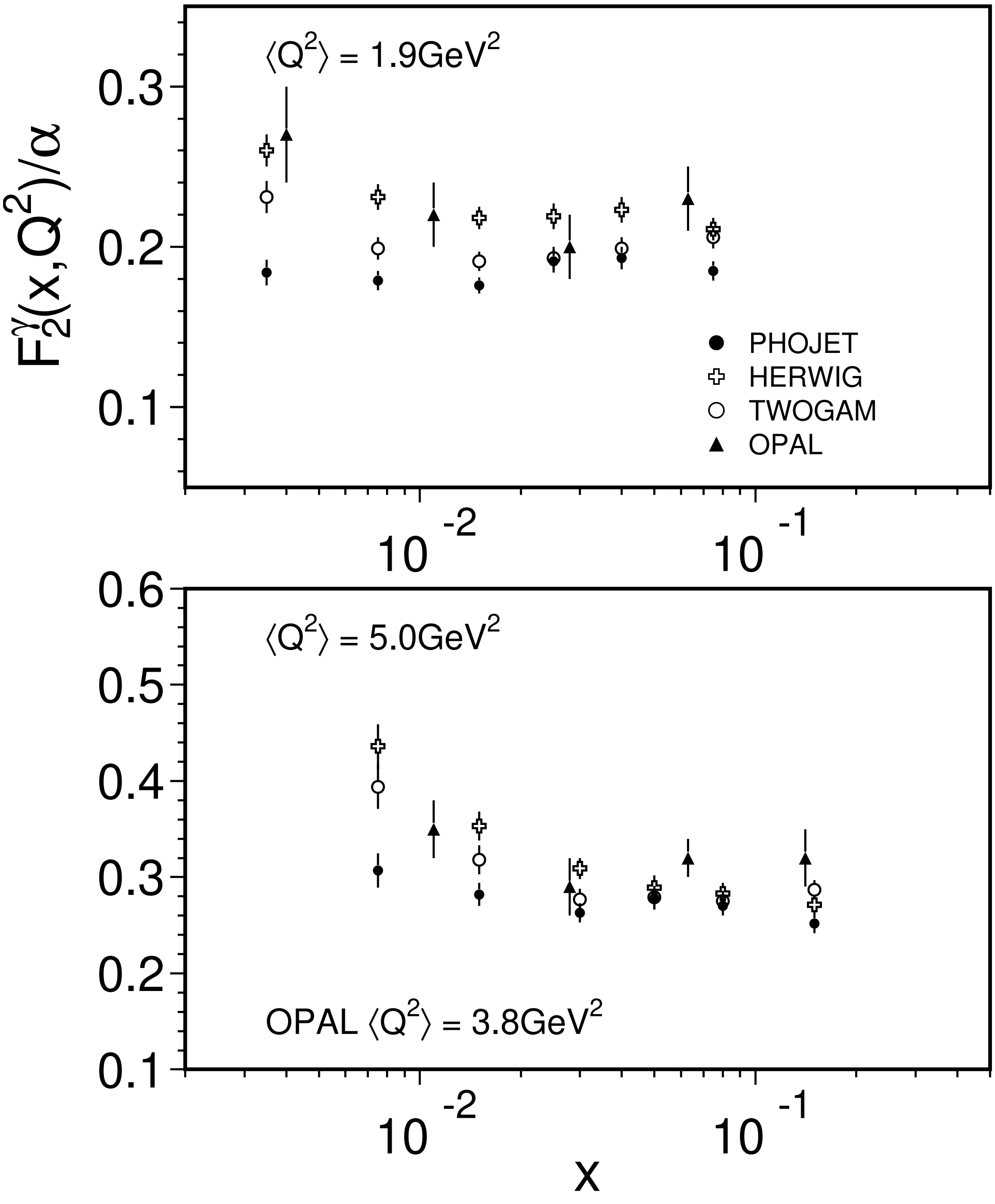

Figure 25: The measured F_2^γ, unfolded with the different Monte Carlos. The OPAL result is also shown.

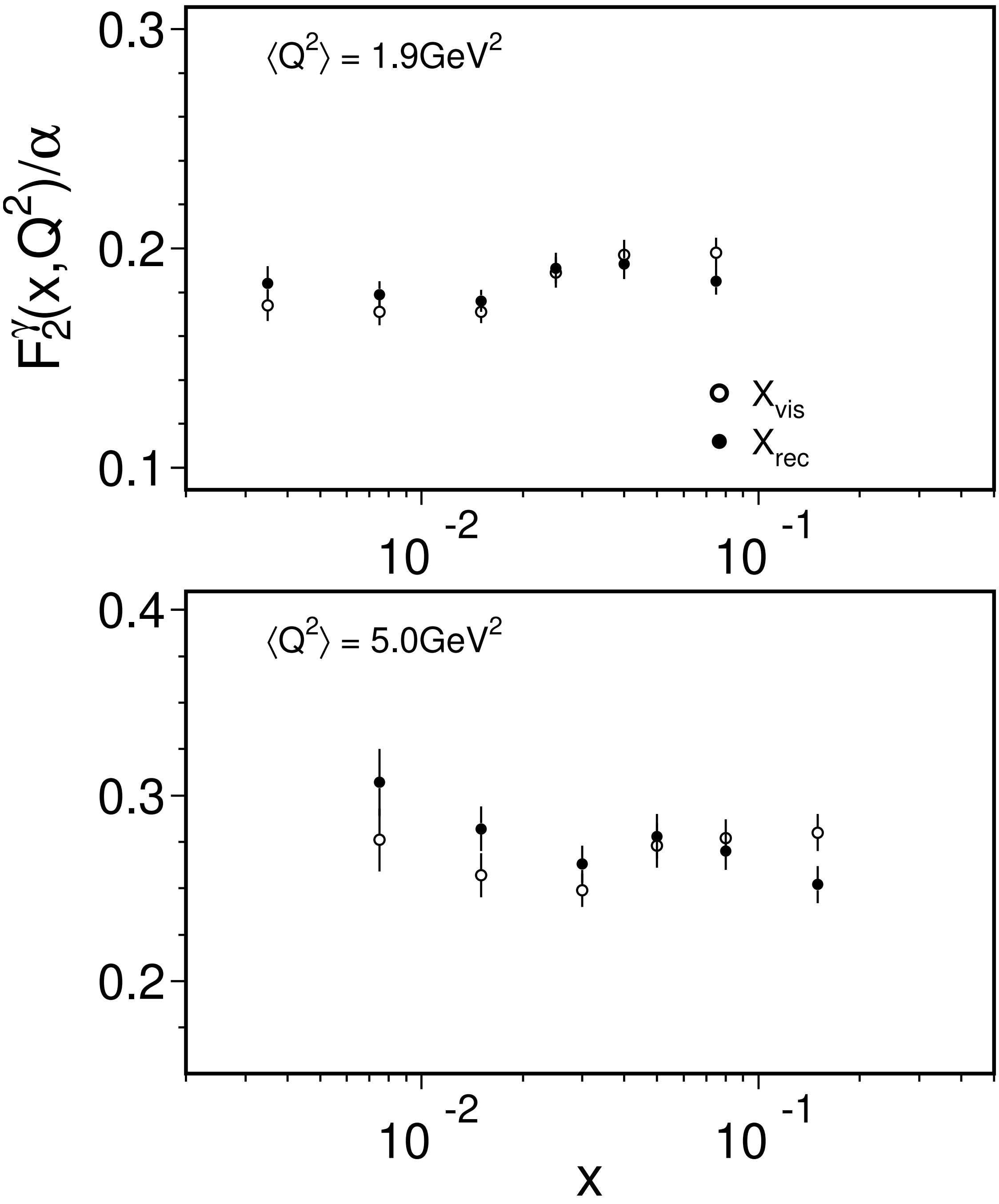

Figure 26: The measured F_2^γ, unfolded from x_{rec} and x_{vis}.

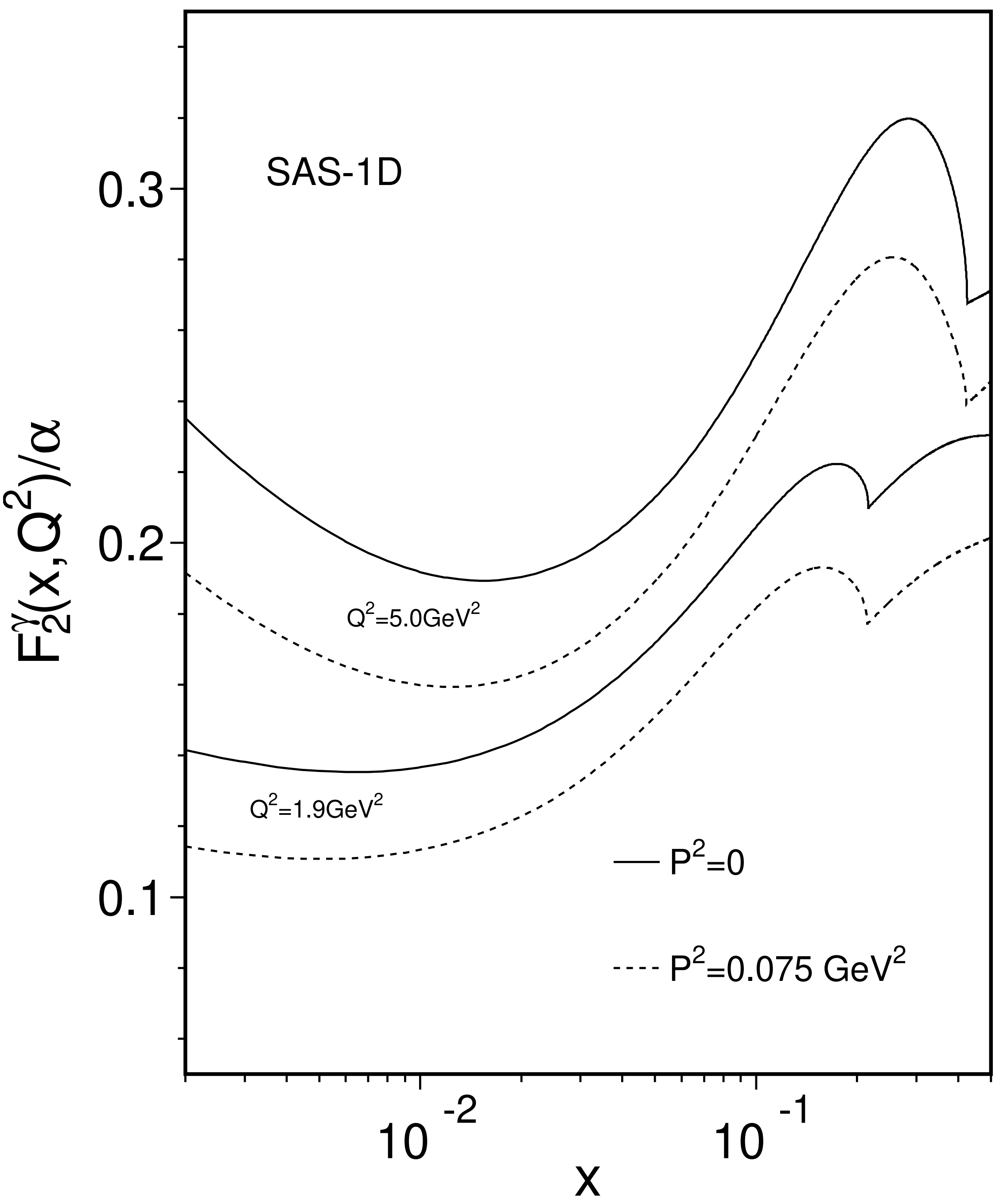

Figure 27: The P^2 dependence of the F_2^γ, predicted by Schuler and T. Sjöstrand [8].

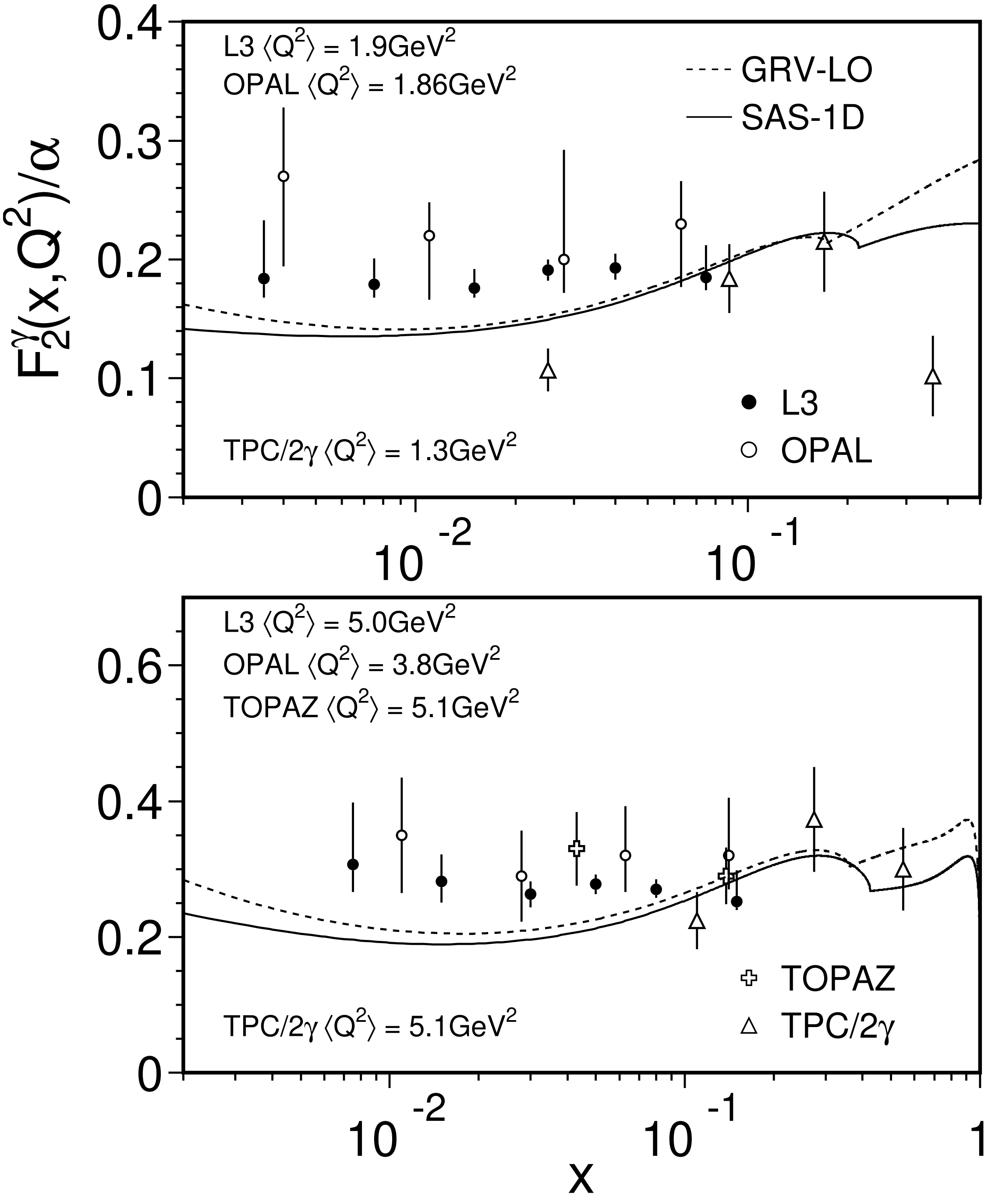

Figure 28: The measured F_2^γ at $\langle Q^2\rangle = 1.9$ GeV^2 and 5.0 GeV^2. Compare with the prediction of GRV-LO and SAS-1d and previous measurements.